Semiconducting TiO_2 for High Performance Ferroelectric Tunnel Junctions

Erik Wikare

Department of Electrical and Information Technology
Lund University

Supervisor: Mattias Borg and Robin Athle

Examiner: Erik Lind

June 27, 2022

Printed in Sweden
Tryckeriet i E-huset, Lund

Abstract

The *ferroelectric tunnel junction* (FTJ) is a rather old concept but has recently been in the spotlight for its promising properties in computer memory technology and neuromorphic computing. The device consists of a ferroelectric insulator sandwiched between two electrodes, and by polarisation switching the resistance along the heterostructure can drastically be adjusted.

The optimisation possibilities of the FTJ are extensive as new materials and processing methods are constantly being discovered. In this thesis, FTJ components will be processed, and an interfacial layer of TiO_2 will be deposited using plasma-enhanced atomic layer deposition between a ferroelectric hafnium zirconate (HZO) layer and electrode to investigate its effect on the performance. Here, the ALD deposition conditions will be altered as well as the TiO_2 layer thickness and placement in the heterostructure. Firstly, the TiO_2 deposition technique will be studied to help understand the impact of the TiO_2 layer.

Several FTJs were fabricated and characterised. The highest remnant polarisation displayed in this thesis was $13.52 \mu C/cm$ with an asymmetric coercive field of -1.7 and 0.9 MV/cm. The TER of the FTJ was 2.9. However, the tool used for HZO deposition was not working correctly during this thesis, but qualitative conclusions could still be made.

Popular Science Summary

Ferroelektricitet upptäcktes först 1921 av professorn Joseph Valasek i kaliumnatriumtartrat, ett ämne som är mer känt som "Rochelle salt". Valasek beskrev likheten mellan ferroelektricitet och det redan då väl beskrivna ferromagnetismen. Likt ferromagnetiska material och deras permanenta magnetiska poler uppvisar ferroelektiska material en permanent elektrisk polarisation, en *separation* av laddningar. På samma sätt som en magnet har en syd- och nordpol, har ferroelektiska material en positiv och en negativ elektriskt laddad pol. Valasek lyckades definiera karakteristiken hos ferroelektriska material långt innan man upptäckte nyttan av dem. Sedan dess har ferroelektriska material funnit sin väg in bland en uppsjö av olika applikationer såsom energiförvaring, sensorer, och ljusavledare.

Även i minnesteknologin har ferroelektriciteten hittat sin plats. Här används laddningsseparationen för att definiera de tillstånd som används vid lagring av data. Här finns det olika möjligheter men fokus i denna uppsats kommer ligga på *the ferroelectric tunnel junction*, förkortat FTJ, som inte riktigt har en bra svensk översättning. I namnet finner vi ordet "tunnel" vilket refererar till det kvantfysikaliska fenomenet "tunneling" som beskriver små partiklars möjlighet att röra sig igenom material av "högre potential". Detta kan liknas med att en boll kastas mot en vägg men istället för att studsa tillbaka hittar vi istället bollen i rummet bakom.

FTJ:n är en elektronisk komponent på nano/mikro skalan som endast består av ett tunt lager av material med ferroelektriska egenskaper som är placerat mellan två elektroder. laddningseparationen, den ferroelektriska dipolen, i det ferroelektriska materialet påverkar den elektroniska uppsättningen i de två elektroderna. Den positiva polen attraherar elektroner och repellerar elektronhål (den positiva motsvarigheten till elektroner). Den negativa polen gör tvärtom. Den elektroniska uppsättningen är viktig för laddningsbärarnas (elektroner och elektronhål) möjlighet att tunnla igenom strukturen. Detta har en direkt påverkan på den ström som kan dras när en spänning placeras över strukturen. Genom att byta håll på den ferroelektriska dipolen kan man påverka den ström som fås. Detta kräver att de elektroder som används påverkas olika mycket av dipolen. Vi får därmed en kontrast i strömmen och två olika minnestillstånd kan representeras.

Acknowledgements

I want to give a special thanks to my supervisor Prof. Mattias Borg for giving me this opportunity and for being an inspiration and mentor. I also want to give a special thanks to my co-supervisor and practical coach Robin Athle whom I have been torturing with questions and issues.

Huge thanks to the other colleagues of the Department of Electrical and Information Technology at Lund University for being very welcoming, kind, and always ready to unlock the door to the lab on the 3rd floor for me.

I need to acknowledge MyFab for its support and access to the Lund Nano Lab.

Finally, I want to thank my office buddies, Albert and Yang, for overflowing these last 20 weeks with laughter and entertaining discussions.

Thank you all!

Abbreviations

ALD	Atomic layer deposition
CVD	Chemical vapour deposition
DI	De-ionised
DRAM	Dynamic random-access memory
FTJ	Ferroelecric tunnel junction
GPC	Growth per cycle
HF	Hydrogen flouride
HfO_2	Hafnium dioxide / hafnia
HZO	Hafnium zirconium oxide
H_2O_2	Hydrogen peroxide
IPA	Isopropyl alcohol
LNL	Lund Nano Lab
MFS	Metal ferroelectric semiconductor
NH_4OH	Ammonium hydroxide
PMA	Post-metallisation anneal
PUND	Positive-Up-Negative-Down
PVD	Physical vapour deposition
RTP	Rapid thermal processing
SiO_2	Silicon dioxide / silica
TDMAHf	Tetrakis(dimethylamido)hafnium
TDMAT	Tetrakis(dimethylamino)titanium
TEMAZr	Tetrakis(ethylmethylamino)zirconium

TER	Tunneling electroresistance
TiO_2	Titanium dioxide / titania
TiN	Titanium nitride / tinite
W	Tungsten

Contents

List of Figures

List of Tables

Chapter 1

Introduction

In an increasingly more data-driven world, new memory technologies are researched, and existing ones are improved. To process and store such huge amounts of data, in this *era of Big Data*, the memories must be ultrafast and energy-efficient while still exhibiting great endurance. The memory cells must also be scalable allowing for high-density integration on the chip.

In machine learning and neuromorphic computing, the ultimate goal is to emulate the human brain using electronic components. The biological synapse, the structure allowing for weighted communication between neurons, can be realised with a two-terminal electronic device exhibiting an analogue conductance states. Similarly to the memory cell, low energy consumption and great endurance are required for such devices.

A new and promising candidate to cross off the beforementioned requirements for both the memory element and synaptic device is the *ferroelectric tunnel junction* (FTJ). The device consists of a ferroelectric insulator sandwiched between two electrodes with an asymmetric charge screening. Carrier transport efficiency through the ferroelectric film depends on the direction of the electric polarisation leading to distinct resistance states. Memory states can thus be represented. The direction of the polarisation, and consequently the conduction, can often be switched gradually. The device can thus emulate a neural synapse.

The device performance is improved if one of the electrodes is semiconducting. The TER, the ratio between highest and lowest resistance, is dramatically increased, allowing for higher contrast between resistance states.

In this thesis, titanium dioxide will be investigated as a possible candidate as the semiconductor electrode of FTJs. Firstly, thin films of TiO_2 will be deposited under varying conditions followed by electrical and optical characterisation. Using the data, deposition conditions giving the optimal characteristics for implementation in FTJs can be determined. Lastly, the FTJ will be processed and evaluated.

Chapter 2

Background

To understand how the FTJs operate and the role of the ferroelectric insulator and semiconducting electrode, the fundamental physics and electronics behind them need to be examined. The processing and characterisation methods used in the thesis work will also be covered, to aid the discussion in later sections.

2.1 Polarisation and Ferroelectricity

From the science of electromagnetism, electric polarisation describes the density of electric dipole moments in a dielectric material. The polarisation is induced by the presence of an electric field that separates the charges slightly in the material resulting in a dipole moment, a *dielectric polarisation*. Stable charge separation is possible due to the insulating property of dielectrics, as opposed to a conductor that would instead conduct a current [1].

The displacement field, $\mathbf{D}$, is defined as

$$\mathbf{D} = \epsilon_0 \mathbf{E} + \mathbf{P} \tag{2.1}$$

where ϵ_0 is the vacuum permittivity, $\mathbf{E}$ is the electric field, and $\mathbf{P}$ is the polarisation. This equation is also known as the *constitutive equation* for electric fields and it describes the separation of free and bound charges. For materials of high dielectric constant, also known as *high-κ* dielectrics, the displacement can be approximated as $\mathbf{D} \approx \mathbf{P}$ [2]. The displacement is also related to the charge scaled by the area of the dielectric. Using the previously mentioned approximation, the magnitude of the polarisation can simply be described as

$$P = \frac{Q}{A} \tag{2.2}$$

where Q is the magnitude of the displaced charges and A is the area [2, 3].

2.1.1 Ferroelectrics

For dielectrics, the electric field and induced polarisation are linearly dependent. Ferroelectric materials, however, demonstrate a non-linearity as well as retaining

a polarisation even when the field is removed, called the *spontaneous polarisation*. Ferroelectrics are also typically characterised by the ability of polarisation reversal by applying an electric field of opposite direction. This is more commonly known as *switching* [3].

A material's possibility of exhibiting ferroelectricity can be expected from its crystalline structure since a fundamental requirement is non-centrosymmetric symmetry. In other words, the crystal is lacking an inversion centre as one of its symmetry elements. An inversion centre can be defined as a point in the crystal lattice through which reflection yields an identical point group - an identical crystal structure. The lack of an inversion centre entails that charged lattice ions are displaced from the centre in the equilibrium state resulting in a net polarisation [4]. With several possible equilibrium states of the charged ion, the crystal may thus adopt several polarisation states of different directions. The switching refers to the reversal of these polarisation directions. In the most simple example, two polarisation states lie on a single axis, causing the switching to be 180°. These ferroelectrics are known as *uniaxial* [5].

2.1.2 Landau-Ginzberg-Devonshire Theory of Phase Transitions

The *Landau Theory of phase transition* is a fundamental theory in the condensed state physics used to describe many physical systems. It is a *phenomenological theory* as it does not concern any interactions at the atomic level, but rather the phenomena and the symmetry changes of the phase transition [6, 7].

A modified Landau theory called the *Landau-Devonshire*, is typically used to describe bulk ferroelectric systems as it simplifies the model by applying a mean-field theory [7]. With a mean-field approximation, long-range interactions are no longer considered and are replaced by a mean value. For thin ferroelectric films, the theory can be modified further to account for any spatial variation in polarisation and potential size effects [6, 7]. The theory is either named *Landau-Devonshire-Ginzberg* or simply *Landau-Ginzberg* in literature.

The Landau theory introduces the Landau free energy, F, a thermodynamic potential much like the Gibbs free energy, that is dependent on thermodynamic variables and external parameters such as the temperature and electric field [8]. The Landau free energy is also dependent on the *order parameter* to take into account the ordering of the phase transition. A first-order is characterised by a discontinuous change in Landau free energy upon transition while for second-order it is continuous [8, 9].

Close to the phase transition, the Landau free energy can be represented with a Taylor polynomial of sixth degree. In the simple case of uniaxial ferroelectrics, the Landau free energy density can be expressed as

$$F_P = F_0 + \frac{1}{2}aP^2 + \frac{1}{4}bP^4 + \frac{1}{6}cP^6 - EP \tag{2.3}$$

where F_0 is the Landau free energy of the unpolarised state. The coefficients, a, b, and c are dependent on various thermodynamic variables. Due to symmetry

reasons of the non-centrosymmetric phase, the odd-powered terms in the Taylor expansion are reduced to zero and are thus not included in the equation. The last term represents the contribution from the applied electrical field, E [10]. From the laws of thermodynamics, the equilibrium state is found by minimising the free energy of the system [3, 10]. Differentiating equation 2.3 with respect to the polarisation and putting it to zero, *i.e.*,

$$\frac{\partial F_P}{\partial P} = 0 \tag{2.4}$$

the following expression can be found

$$E = aP + bP^3 + cP^5. \tag{2.5}$$

The coefficients, a, b, and c, are of great importance for the behaviour of the phase transition. A simplification introduced by the Landau-Devonshire theory is that only the first coefficient, a, is dependent on the temperature, T and that it follows the Curie-Weiss law [3, 10]:

$$a = a_0(T - T_0) \tag{2.6}$$

where a_0 is a positive constant and T_0 is the *Curie temperature*. The sign of the second coefficient, b, directly implies whether the phase transition is of the first or second order. For first-order reactions the second coefficient is negative and for second-order reactions the coefficient is positive [3].

In figure 2.1, the Landau free energy is plotted against the polarisation for the first order reactions without an external electrical field. For positive a, only one minimum is displayed at zero polarisation. For negative a, meaning that we are below the Curie temperature, the curve displays two minima at non-zero polarisation [10].

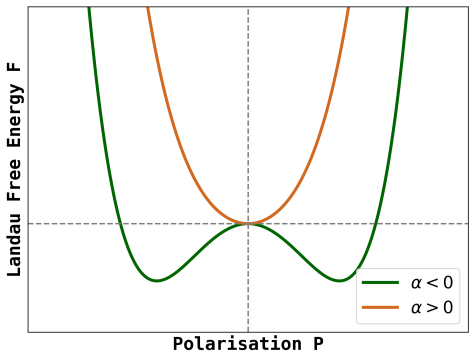

Figure 2.1: The Landau free energy as a function of polarisation given by equation 2.3 and $E = 0$.

Since the equilibrium states are found by minimising the free energy, the curve indicates thus that two polarisation states exist (at equilibrium) [3, 10]. In this

case, the two polarisation states are of equal magnitude but opposite signs and represent the two dipole directions of the uniaxial ferroelectric. The non-zero polarisation at zero electric fields is one of the characteristic features of ferroelectrics, the previously mentioned spontaneous polarisation. Due to the energy barrier between the two minima, the polarisation is hindered from "jumping" between the two states and will remain in one of the states [10].

2.1.3 Ferroelectric Domains

As with all ferroics, ferroelectric materials are typically composed of several *domains* in which the spontaneous polarisation is aligned. Separating these domains of different directions is an interface called the *domain wall* and is typically only 1-2 unit cells wide [11]. The driving force for the formation of such domains is to minimise strain energy and achieve net neutrality in the material. The countering force is the energy needed for domain wall formation as it introduces interfaces in the crystal [3].

2.1.4 Polarisation Reversal - Switching

As indicated by the last term in equation 2.3, an external electrical field would modify the Landau free energy curve with the term $-EP$. Since this is a purely linear term the two minima are shifted according to as depicted in figure 2.2. Above a certain electrical field, only one out of the two minima is present and thus only one polarisation state can be found at equilibrium. *Vice versa* occurs with a field of opposite sign. Alternating between the two directions of the electric field, the direction of the polarisation is switched accordingly. These are the basics of ferroelectric switching. [7, 10, 3] A fundamental requirement of ferroelectrics is the possibility of switching before a dielectric breakdown. The polarisation is in this case called *reorientable*. At high fields, the insulating property may be lost and the material will act as a conductor. The material can no longer uphold a polarisation [2].

Switching by applying an electric field increases thus the fraction of domains of aligned polarisation. This can happen in two ways: *domain wall motion* and *nucleation*. Domain wall motion refers to the expansion of domains with polarisation aligned with the electric field, while nucleation simply refers to new domains forming. Both mechanisms occur simultaneously in a ferroelectric component [3], however, nucleation-limited is preferred as it allows for faster switching [12].

2.1.5 The PE Curve

Ferroelectrics are characterised by its *Polarisation-Electric field curve*, or "PE curve" for short. The curve is given by equation 2.5 and is shown in figure 2.3. In real experiments, the ferroelectric materials typically only exhibit one polarisation state. Thus the observed response follows the solid line instead of the dashed. The polarisation response on the electric field is a hysteresis loop, a fundamental response of ferroelectrics [3].

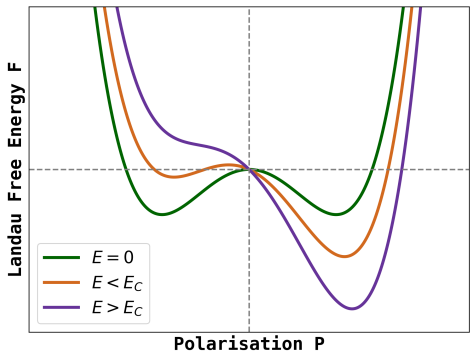

Figure 2.2: Landau free energy landscape for three different cases of applied electrical field. At field above the coercive field, only one minimum is present.

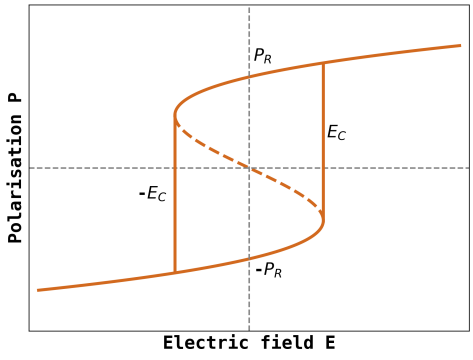

Figure 2.3: Polarisation as a function of electrical field including the remnent polarisation P_R and coercive field E_C.

From the hysteresis loop, two important characteristic properties of the ferroelectric material, the *remnant polarisation* P_R and *coercive field* E_C, can be identified. P_R can be found as the non-zero polarisation after switching when the electric field has been reduced to zero. The remnant polarisation is thus equivalent to the spontaneous polarisation. E_C can be found as the minimum electric field that is needed to switch the polarisation state. This is thus the field at which the Landau free energy curve only contains one minimum, as discussed in the previous section. For real ferroelectric materials, however, the switching typically occurs over a range of electric fields. A high remnant polarisation and steep range of the coercive field is an indication of a high fraction of aligned ferroelectric domains in the material [1, 2].

2.1.6 Wake-up and Fatigue

During continuous cycling of the polarisation states, the hysteresis loop of the ferroelectric may undergo changes. These observed changes can be collected under two blanket terms, *wake-up* and *fatigue* [13].

Wake-up occurs during the initial cycles and is often identified with an increase in the remnant polarisation. The processes behind the wake-up are not entirely established but a few have been suggested and some proven. Firstly, repeated switching may redistribute oxygen vacancies that were formed during deposition. These vacancies, and other defects, can be seen as obstacles to the domain wall motion and by so causing *domain pinning*. Since switching occurs partly via domain wall motion, the polarisation response to the field is thus reduced. The redistribution of oxygen vacancies can also increase the fraction of the ferroelectric phase in the crystal by enabling phase transitions from non-ferroelectric phases [14]. *Ferroelastic* switching may also be a process behind the observed wake-up effect. This type of switching effectively reorients domains whose polar axis is not aligned with the axis of the electric field. Typically a high electric field is needed for this to occur. Strain is also induced in the material since the lattice parameters of the crystal are most likely different [13].

Fatigue occurs during a higher number of cycles and is identified with a decrease in remnant polarisation. Similar to the wake-up process, the underlying mechanisms are not entirely established. The high repetition of cycling increases the defect concentration in the material and is thus believed to increase the domain pinning. The increased defect concentration eventually culminates into highly conductive paths and finally dielectric breakdown [13, 15].

2.1.7 Ferroelectric Hafnium Oxide

Hafnium oxide-based thin films have been widely used in the semiconductor industry as a dielectric due to their high dielectric constant and compatibility with silicon CMOS technology [16].

Recently, ferroelectric properties have been discovered in doped HfO_2 [17, 18]. The ferroelectric phase is of an orthorhombic crystal structure, space group $Pca2_1$, that is typically called the *O-phase*. The structure is illustrated in figure 2.4.

Four of the negatively charged oxygen ions have two equilibrium positions in the space bounded by the hafnium atoms. Both positions lie off-centre causing a displacement of charges in the unit cell; it is non-centrosymmetric and polar. It can exhibit ferroelectricity. In this case, the ferroelectricity is *uniaxial* in that the polarisation switches along a single axis [3].

The orthorhombic phase is a metastable phase and is thus typically not adopted by the oxide in nature and must be induced. A successful method is to cap the oxide with a material that exerts mechanical stress [19] while the structure is annealed to high temperatures due to differences in thermal expansion coefficients. This is typically called a *post-metallisation annealing* (PMA) treatment [20]. For thin films, the ferroelectric phase is further promoted by doping, and several dopants such as lanthanum, silicon and zirconium can be used. By doping the PMA temperature can be drastically lowered [21]. Zirconium-doped hafnium, also called hafnium zirconate, shows great and robust ferroelectric properties such as high remanent polarisation. Experimental studies have shown that around a 1:1 ratio of hafnium and zirconium results in the strongest ferroelectric properties [22]. At lower doping concentration, a monoclinic phase called the "m-phase" is stabilised, while for higher concentrations a tetragonal called the "t-phase" forms. The m-phase and t-phase are neither ferroelectric but paraelectric and antiferroelectric, respectively. Increasing the fraction of the ferroelectric phase promotes the ferroelectric properties [22, 23, 18, 24].

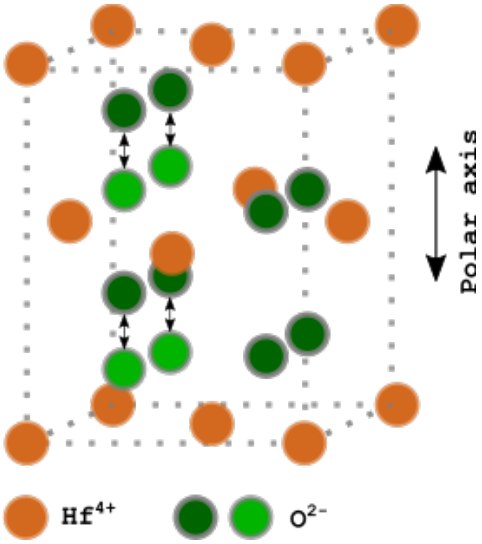

Figure 2.4: The ferroelectric orthorombic phase of HfO_2. The figure shows two equilibrium positions of the oxygen ions in the lattice resulting in two polarisation states along the polar axis.

2.2 Ferroelectric Tunnel Junction

As briefly mentioned in the introduction, the ferroelectric tunnel junction is a promising component for both memory technology and neuromorphic computing. A simple FTJ is realised by growing a thin layer of a ferroelectric insulator between two metal electrodes; *i..e* a metal-ferroelectric-metal (MFM or MIM) structure. Carrier transport efficiency through the insulator is dependent on the direction of the polarisation allowing for discrete resistive states. High resistance contrast is achieved by replacing one of the metal electrodes with a semiconducting material, *i.e.* an metal-ferroelectric-semiconductor (MFS) structure [25].

Charge carrier transport through the ferroelectric insulator is mainly through three mechanisms, thermionic injection (TI), Fowler-Nordheim tunnelling (FNT), and direct tunnelling (DT). Quantum tunnelling is the phenomenon of small particles travelling across thin barriers of higher energy than the particle, something that is not possible in classical physics [26]. The ferroelectric insulator in the FTJ can be represented by such as barrier and tunnelling can occur if the layer is thin enough. As hinted by its name, direct tunnelling represents the charge carriers that tunnel through the barrier directly. Fowler-Nordheim tunnelling represents charge carriers that tunnel through a thinner barrier due to the barrier modulation caused by the applied voltage. This mechanism is primarily prevalent when high voltages are used. Thermionic injection represents those electrons of high enough thermal energy to pass over the barrier [27].

Figure 2.5 illustrates the MFS FTJ and its bandstructure when the polarisation has been switched completely in the two directions. This is the case of n-doped semiconductor. When the direction of the polarisation is towards the metal electrode, the small negative pole repels the negative charge carriers, the electrons, in the semiconductor. This is analogous to an upward bending of the semiconductor bands, as shown in the figure. This phenomenon is conventionally called *depletion* effectively resulting in an *Schottky barrier* [28]. With polarisation pointing in the other direction, the negative electrons are attracted instead and a downwards band bending happens. In this case, no change in barrier width has occurred [25].

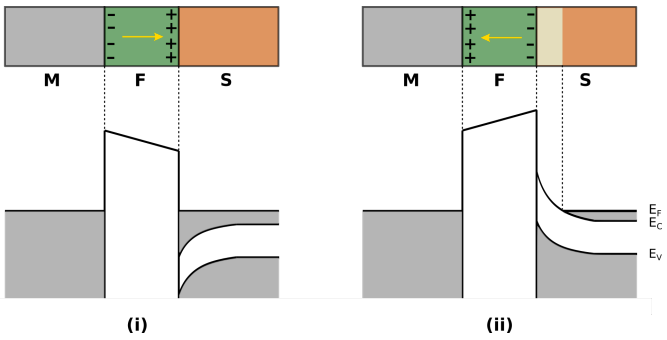

Figure 2.5: Schematic of the metal-ferroelectric insulator-semiconductor (MFS) heterostructure and the corresponding bandstructure at the two polarisation states of the ferroelectric. The semiconductor is n-doped.

The direct tunnelling current density, J_{DT}, for a MIM FTJ can be expressed as

$$J_{DT} = C\frac{\exp[\alpha((\Phi_{B,2} - \frac{eV}{2}))^{3/2} - (\Phi_{B,1} + \frac{eV}{2})^{3/2}]}{\alpha^2[\sqrt{\Phi_{B,2} - \frac{eV}{2}} - \sqrt{\Phi_{B,1} + \frac{eV}{2}}]^2} \times \sinh[\frac{3eV}{4}\alpha(\sqrt{\Phi_{B,2} - \frac{eV}{2}} - \sqrt{\Phi_{B,1} + \frac{eV}{2}})] \tag{2.7}$$

$$\left[C = -\frac{4em_{e,oxide}}{9\pi^2\hbar^3} \quad , \quad \alpha = \frac{4d\sqrt{2m_{e,oxide}}}{3\hbar(\Phi_{B,1} + eV - \Phi_{B,2})}\right] \tag{2.8}$$

where $\Phi_{B,1}$ and $\Phi_{B,2}$ are the potential barriers at the interfaces, e is the electron charge, and $m_{e,oxide}$ is the effective electron mass in the oxide. V is the applied voltage over the junction [27, 29]. As shown in figure 2.6 and by the equation, the tunnelling current is exponentially dependent on the barrier width, d.

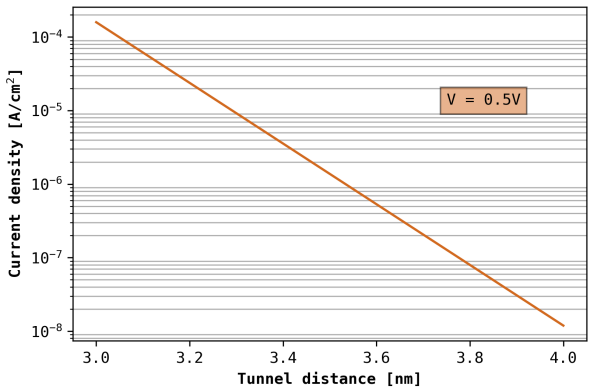

Figure 2.6: The current density as a function of the tunnel distance at an applied voltage of 0.5V. The following parameters are used in the simulation: $\Phi_{B,1} = \Phi_{B,2} = 1eV$, and $m_{e,oxide} = m_e = 9.109E - 31$kg

Applying this to the MFS FTJ, the increased barrier width due to depletion of charge carriers in the semiconductor results thus in an exponentially smaller tunnelling current. A high resistance contrast, also called tunnelling electroresistance TER, is achieved between the two polarisation directions [29]. The state of highest resistance and lowest resistance is typically called the *high-resistive state* (HRS) and *low-restive state* (LRS). The TER can be identified as the ratio between the current prior and post switching. The modulation of the barrier width, Δd, can be compared to that of the depletion width of a Schottky diode:

$$\Delta d = \sqrt{\frac{2\epsilon_s(V_{bi} - V)}{qN_D}} \tag{2.9}$$

where ϵ_s is the dielectric constant of the semiconductor, V_{bi} is a *built in voltage*, and N_D is the donor doping concentration [30]. The TER is thus dependent on the dielectric constant of the semiconductor and doping concentrations.

Thermionic injection and Fowler-Nordheim tunnelling lack such an exponential dependence on the barrier width and should thus not dominate for high TER in MFS FTJs. For the direct tunnelling to dominate the layer must be very thin, in order of some nanometers [27].

2.2.1 The Memristor

Together with the capacitor, inductor, and resistor, the memristor is one of the four fundamental two-terminal circuit elements. The four elements and their relationship is shown in figure 2.7. The name "memristor" is a portmanteau of the words "memory" and "resistor" as it behaves like a resistor with a memory. [31] The memristance relates the flux-linkage with the charge variable through a memristance, M, by

$$d\phi = Mdq \tag{2.10}$$

where ϕ is the flux-linkage and q is the charge. The equation points to an integral relationship between the state variables of the memristive systems, and a memristance that is a function of the integrated current. The memristance is thus dependent on the current that has passed through - a memory effect [31, 32].

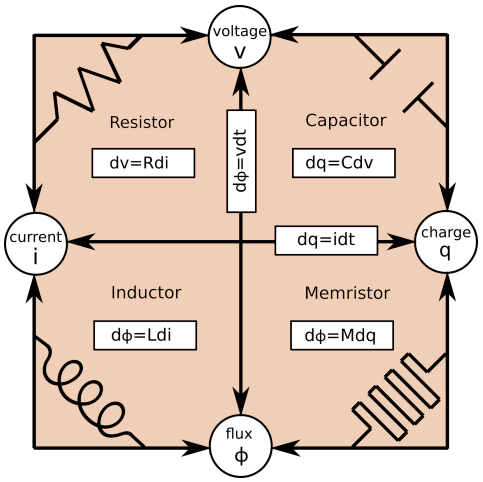

Figure 2.7: The four fundamental two-terminal circuit elements; the resistor, capictor, inductor, and the memristor. The figure show their relationship to each other via the state variables.

As mentioned in section 2.1.3, polarisation reversal of a ferroelectric is the action of increasing the fraction of domains of which the polarisation is aligned with the applied electrical field. The gradual increase in aligned domains imply that the junction resistance of the FTJ can be controlled over a range of resistance levels

[33]. This is also called partial polarisation reversal. The FTJ thus shows memristive behaviour. The memristive behaviour is necessary and the fundamental property that allows the FTJ to work as both a multistate memory and artificial synapse [32].

2.2.2 FTJs as Memory Element

The observed performance of the FTJs is of great interest as it could possibly fulfil the requirements of the next generation of computer memory elements. The performance is characterised by the switching time, energy consumption, cycling endurance, and *retention*. The memory elements are further characterised by their *volatility*, readout operation, scalability, and eventual multilevel state representation [12]. Owing to the FTJ's great performance is the physics of the polarisation-dependent resistive-type operations of write and readout [34].

The switching time is directly dependent on the switching operation of the FTJ. As mentioned earlier, the polarisation reversal in the thin layer can either occur via the nucleation or domain-wall motion model [12]. Fastest switching have been observed for nucleation-limited reversals, reaching down to the sub-nanosecond regime. In these cases, the switching time is limited by the experimental setup or in the most extreme case by the phonon frequencies [35]. Since the memory state is determined by an applied electrical field, instead of a current as for many other type of memory, the energy efficiency of FTJs has great potential. The energy consumption can be estimated to below 10 fJ per switch [12]. The cycling endurance is dependent on the before-mentioned fatigue and dielectric breakdown caused by primarily defect formation. However, studies has shown that sufficient cycling is possible [35]. A common problem with ferroelectrics is insufficient charge compensation at interfaces causing the polarisation to degrade. This affects the retention which describes the memory cell's ability to retain any polarisation state. Studies has shown, however, that depolarisation in FTJs and thus retention is not a problem [12, 35].

The volatility describes whether the memory cell retains the memory state once power has been cut. The memory cell may either be volatile, *i.e.* the memory is lost, or non-volatile, *i.e.* the memory is saved. Since the equilibrium state is separated by an energy barrier, as shown in figure 2.1, non-volatility is ensured. The polarisation state does not need a supply of current or voltage to retain, which is the definition of the spontaneous polarisation. Non-volatiliy is a common feature of resistive-type memories. The switching at coercive fields or higher also enables *non-destructive* readouts by using read-voltages below this critical point [34, 35]. As mentioned earlier, the current through the FTJ is exponentially dependent on the tunnelling barrier width. This is what makes it possible to achieve such a high TER. Additionally, as a result of this highly non-linear IV characteristic, the ultimate scalability of the FTJ is equal to $4F^2$ [34]. F is the smallest feature size that can be fabricated and is, for example, equal to the wavelength of light used in lithography, a process which will be brought up in the next section [30]. $4F^2$ is the ideal 2D memory cell size; the scalability of FTJs is thus excellent. The simple architecture of the FTJ could also allow for efficient 3D packing. The

possibility of multistate representation in the FTJ due to the gradual increase of aligned domains was already mentioned in previous section. This can however limit the scalability since several domains are needed for multistate representation. In the increasingly more data-driven world, modern workloads require huge storage capacities and efficient data processing. With today's computer architecture, the *von Neumann model*, the data storage and processing are separated, creating a need for efficient data transfer between the two as well. The development of data transfer has however not kept the same pace as the processing and memory leading to undesired latency. This limitation of the data handling is also called the *von Neumann bottleneck*. The memristive behaviour of the FTJ, and other resistive type memory elements, can be the solution to this problem. The solution is in-memory computation in which data processing and storage can be kept at the same place, thus completely avoiding the need for transfer [36].

2.2.3 FTJs as Artificial Synapse in Neuromorphic Computing

The brain and its minimal power consumption and extreme processing power can be seen as the blueprint for the ultimate supercomputers. The operating principles of the human brain need thus to be mimicked, which is the basis of *neuromorphic computing* [37]. A fundamental principle of the human brain is the electrical spike transmission between neurons in the so-called synapse. In short, by adjusting the strength of these transmissions, also called the weight, the human brain learns. This is also called *synaptic plasticity*. An ultrafast, energy-efficient, nanoscale memristive device has the possibility of emulating the works of a synapse as the weight can be represented by the resistance (or more intuitively the conductance). The conductance of the memristor is dependent on the history of applied voltage and thus plasticity is ensured [37, 38].

The FTJ is a candidate to be implemented as the synaptic device in artificial neural networks due to the partial polarisation reversal that allows for a continuous range of resistance (or conductance states). The synaptic weight can be represented [24]. Plasticity has been observed in FTJs as the partial polarisation is dependent on both the amplitude and width of the voltage spikes [39]. However, as mentioned in the previous section, the multilevel representation can be lost as the 2D scaling of the FTJ reaches down to ferroelectric domain size. The continuous range of resistance levels and thus synaptic weight, is lost. Ferroelectric switching is, however, probabilistic and allows for synaptic weight updates through stochastic switching [40].

2.3 Processing Methods

In this section, relevant tools for the fabrication and evaluation of ferroelectric tunnel junctions will be described. In microfabrication, typically several "bottom-up" and "top-down" processing step is needed for both the component and any connected circuitry.

2.3.1 Atomic Layer Deposition

Atomic layer deposition belongs to the family of chemical vapour deposition (CVD) techniques as the film formation occurs via reaction of vaporised reactants. The technique allows for high film uniformity, and thickness and composition control on the atomic level [30, 41]. The basic principle of ALD is sequential exposure of chemical reactants, as shown in figure 2.8. ALD differs thus from conventional CVD where a continuous supply of the reactants is dosed onto the sample simultaneously. By so, chemical reactions can only take place on the sample surface and once fully covered the deposition is saturated. This self-limiting deposition of only one monolayer is what allows for precise thickness control [42].

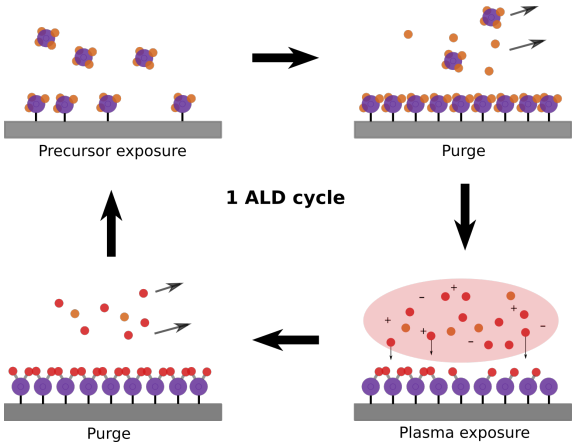

Figure 2.8: Illustration of the four steps that comprises one ALD cycle. The figure includes an example of chemical reactants, and does not necessarily depict a real example.

In addition to the chemical reactant pulses, a typical ALD cycle also contain two purge steps to remove unused reactants and reaction products. Naturally, this is carried out with a flow of an inert gas such as nitrogen or argon after dosage of each chemical reactant [42]. The inert gas is often also used as a carrier gas for the chemical reactants. The cycle is repeated until the desired film thickness is achieved. The process is often characterised by the deposition rate in Å/cycle, its *growth per cycle* (GPC) [30].

To achieve thickness control the sample surface needs to be fully saturated by the chemical reactants. Saturation is ensured by using long enough pulse and purge times and by using an appropriate temperature. In figure 2.9, the temperature

dependence of the GPC is shown. At too low and too high temperatures, the deposition is imperfect leaving behind a so-called "ALD window" at intermediate temperatures. Here the GPC is constant at one monolayer per cycle. At too low temperatures, insufficient energy is available for the reactions resulting in limited kinetics and even precursor condensation. At too high temperatures, precursor decomposition and desorption occur instead [30]. Precursor decomposition involves the breakage of weak molecular bonds [43] above the sample surface leading to uncontrolled deposition [44].

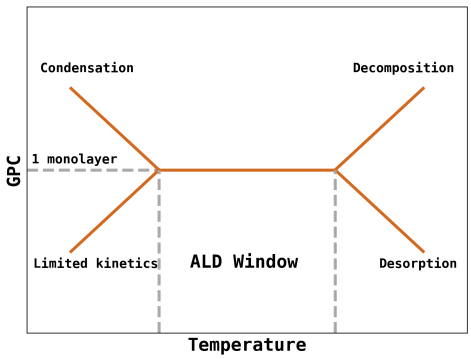

Figure 2.9: A schematic of the dependence of the growth per cycle (GPC) on the deposition temperature. The figure shows a temperature interval of constant GPC of 1 monolayer, called the ALD window.

To decrease the temperature needed and to also introduce new precursors to the world of ALD, plasma can be used in the oxidising step. The technique is reasonably called plasma-enhanced ALD. Due to a high content of ions and radicals in the plasma, it is highly reactive and thus allows for the previously mentioned advances. Oxygen and nitrogen gas are typically used as plasma sources. The plasma is ignited using a radio frequency electric field to tear apart the charges in the gas. The plasma can be generated remotely to only be dosed over the sample, to protect the sample from the high-energy ions [45, 46].

2.3.2 Photolithography

Photolithography is a processing technique used to create patterns in thin films. In the process, a light-sensitive polymer material, called a *photoresist*, is exposed to light. A mask containing the wanted pattern is installed to block parts of the light and thus the pattern is transferred to the resist. This is illustrated in figure 2.10. By dipping the photoresist in a development solution, the resist is dissolved, washed away, and leaving behind the patterned structure [30, 47].

Depending on its response to the light, a photoresist may be classified as positive or negative. Exposed positive photoresists become more soluble while negative resists harden. During the development, the exposed positive resist is thus washed away, and the mask pattern and transferred pattern are the same. For negative resists, the exposed resist remains, and the transferred pattern is "inverted". [30] The resist is typically spun onto the sample using a spinner. In this way, an acceptable uniform thickness is attainable, and the thickness can be controlled using the spin speed and time [30]. After spinning, the resist is *prebaked* to promote adhesion and to release any built-in stress. The prebake also hardens the resist by evaporation of solvents [47].

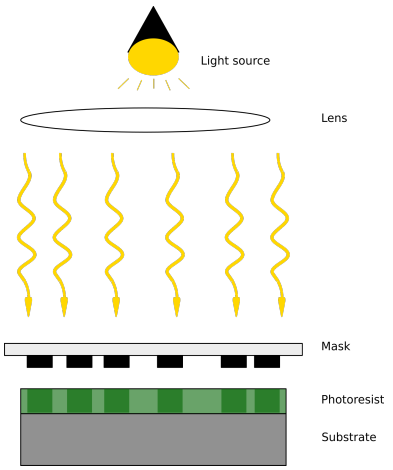

Figure 2.10: Illustration of the patterning of a light sensitive material in photolithography.

2.3.3 Wet Chemical Etching

Wet chemical etching is a material-removing method used either for contamination cleaning or for selective removal of surface layers. In the latter, etchant-resilient masks can be used to define structures in the etched film. Such masks can be achieved using photolithography [30, 48]. A great adhesion between the film and photoresist is in that case beneficial.

2.3.4 Metallisation: Sputtering and Evaporation

Evaporation and sputtering are two of a few methods for the deposition of films of metals and compounds. Both belong to the family of physical vapour deposition (PVD) techniques, in that the metal or compound does not react upon deposition. High-vacuum is typically used in these systems to avoid contamination of any gas molecules. The thickness of the thin film can be monitored during the processes using a quartz microbalance [23, 49].

Sputtering

In sputtering, a metal source is subjected to a bombardment of high energy particles causing metal atoms or even clusters to be ejected from the surface. The atoms travel through the chamber vacuum and are deposited on the surface of the sample. Plasma can be used as a source of such high energy particles and is typically formed from a gas of inert species of high molecular weight, such as Argon. High voltages tear the electrons apart from their host atoms leaving them positively charged. As shown in figure 2.11i, the anode lies behind the sputtering target and accelerates the positively charged particles to the target. Magnetrons with strong magnetic fields are typically utilised to confine the plasma close to the target, thus avoiding any damage to the sample and also creating a high-density plasma [41].

The magnetrons supply the electric field needed to form the plasma and can either be direct current (DC) or radiofrequency (RF) powered. Direct current only works for conducting materials and radiofrequency for non-conducting. If direct current powered, a depolarisation field would occur on the surface of the non-conducting target due to accumulation of positive plasma ions. An alternating fields prevents thus this [50].

Evaporation

In evaporation processes, the metal source is heated to produce vapour either through evaporation or sublimation. The vapour transfers atoms from the source to the sample surface. Direct resistance, electron beam, and laser beam are a few examples of means of heating. Evaporation through electron beam has its advantages over the other methods such as cleaner deposition, faster [51] and more controllable deposition rates [49].

Figure 2.11ii illustrates the basics of the electron beam evaporator. The beam is produced by an electron gun consisting of an anode and cathode powered by a strong electrical field. The electrons are accelerated by the field and travel with high energy to the metal source. Since electrons scatter easily by gas molecules, the high vacuum in the crucible is important. To produce and control the electron beam would otherwise be restricted. The energy of the electron beam is transferred to the metal and converted to thermal energy. The sample holder is placed above the metal source and condensates the vapour resulting in film formation [49].

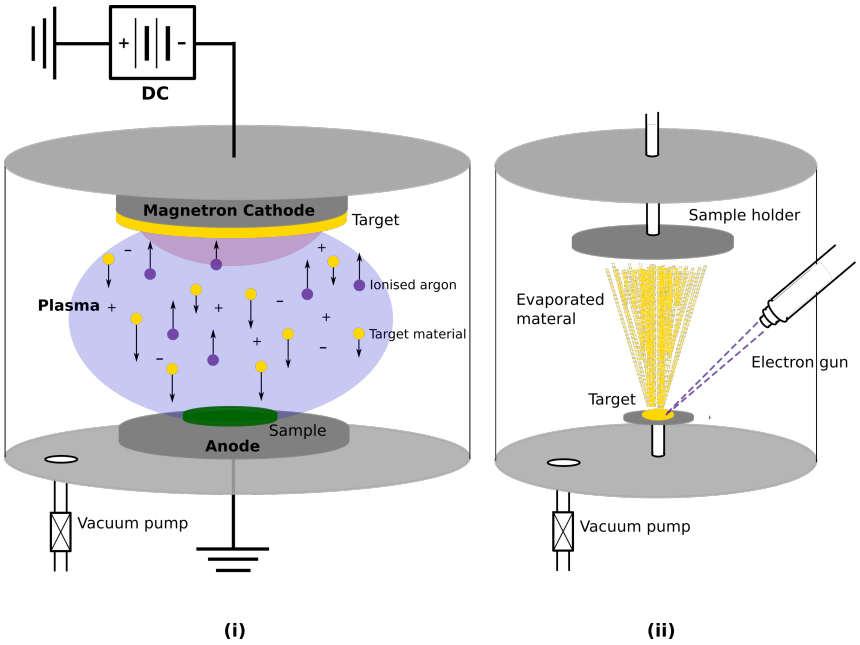

Figure 2.11: A schematic of **(i)** a sputterer and **(ii)** an electron beam evaporator used for thin film deposition.

2.4 Characterisation Methods

2.4.1 Spectral Ellipsometry

Ellipsometry is an optical characterisation method used to determine the refractive index, thickness, roughness, and uniformity of thin films. The ellipsometer measures the change in polarisation as linearly polarised light is reflected onto the sample at different angles and over a range of wavelengths [52].

Any polarisation state can be represented with two orthogonal vectors, the *s and p components*. The reflected light is elliptically polarised and can be represented as a rotation, ψ, and phase shift, δ, of the s and p components, see figure 2.12. The change in polarisation upon reflection is dependent on the sample thickness and optical properties [53].

However, the correlation between the film thickness and the measured change in polarisation is intricate. A regression model is therefore used to fit the acquired data to an existing model. Ellipsometry is, thus, an indirect measurement method. The deviation between experimental and model is measured as an MSE (mean square error) and should, naturally, be as low as possible. [53] Although indirect, the properties can be accurately determined by using appropriate models [52].

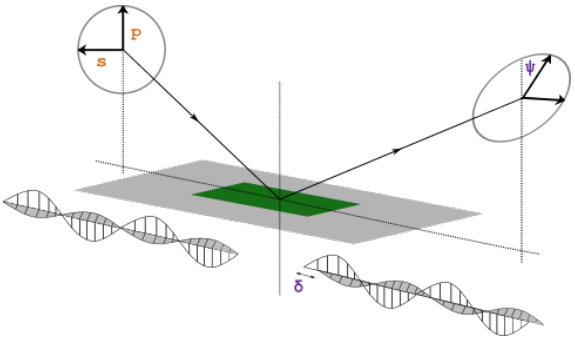

Figure 2.12: The change in polarisation upon reflection on a sample. This is utilised in spectral ellipsometry.

2.4.2 Four-probe Method

A common way to measure to resistivity of thin semiconductor films is the four-probe method. The basic principles behind the method is to source a current between the outer probes and measuring the voltage drop between the inner. By doing so, the contact resistance is excluded since no current is drawn by the inner probes.

2.4.3 PUND Method

The standard method of characterising the ferroelectric response is the *PUND method*. The principle behind the method is to distinguish the current produced as the ferroelectric polarisation is switched in the material. This is possible by applying a voltage pulse train consisting of two positive pulses followed by two negatives. The four pulses are called the *positive-up-negative-down* and gives the method its name. In the first pulse, "P", the ferroelectric polarisation is switched and the current is produced by the charge displacement. A capacitive and leakage current is also produced and thus the ferroelectric current cannot be identified. These unwanted currents are naturally the largest at the highest applied voltage, while the ferroelectric current response should lie around a bias corresponding to the coercive field. Since the polarisation is retained by the ferroelectric material, the following pulse of the equal sign, "U", does not include the ferroelectric current. By subtracting the current produced by the two pulses, only the ferroelectric current remains. The same logic is applied to the two last pulses, "N" and "D". [3] The PUND scheme is shown in figure 2.13 and is typically initiated with a pulse to set the polarisation to one direction.

The polarisation response can be calculated from the current produced by the polarisation switching. The polarisation density was defined by equation 2.2 in section 2.1. Since the total charge is the integral of the current I, the polarisation response of the ferroelectric can be expressed as

$$P = \frac{Q(V)}{A} = \frac{1}{A}\int_t I(t)\ dt \tag{2.11}$$

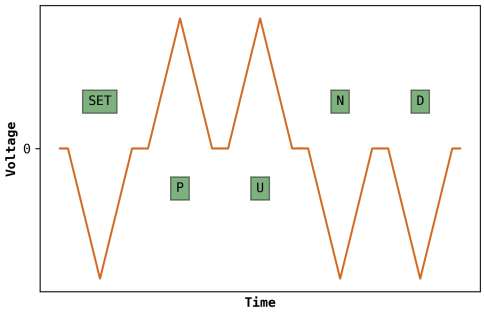

Figure 2.13: The voltage scheme used in PUND measurements.

and the PE hysteresis curve can be plotted [3].

Chapter 3

Processing and Characterisation

In this chapter, the processing and characterisation steps of the titanium dioxide thin films and ferroelectric tunnel junctions will be presented. The steps will contain the methods mentioned in the previous chapter.

3.1 Titanium Dioxide Thin Films

A 2-inch silicon wafer with an overlayer of SiO_2 was used as the substrate for the TiO_2 films. Before deposition, a model of the SiO_2 overlayer was constructed in the Woollam RC2 ellipsometer in LNL to ensure acceptable measurements of the subsequent TiO_2. The wafer was also cut into smaller pieces.

The deposition of TiO_2 was carried out using the Cambridge Nanotech Fiji F200 ALD tool in LNL. TDMAT was used as the titanium precursor, oxygen plasma as reactant, and Argon as carrier gas. The plasma was generated by Industrial Power Systems Seren AT3 at 13.56 MHz and 300 W. Several samples were grown and the plasma exposure time, precursor pulse length, and temperature were altered for three separated experiment series. For all depositions, the number of cycles was 200 and the purge time was 5 seconds long.

The thickness and refractive index of each of the samples were measured on six points with the ellipsometer. The data was measured at three angles; 60°, 65°, and 75°. The data was used to calculate the GPC.

3.1.1 Four-probe Measurements

The resistivity of the TiO_2 layer for each of the samples was measured using the four-probe method (4P). A series of processing steps were needed to create the 4P structure. In figure 3.1, an illustration of the sample during several of the processing steps is shown. Figure 3.1i represents the structure attained directly after the ALD.

Firstly, the samples were cut into approximately 1x1 cm dies and then cleaned by a 30 seconds stir of acetone followed by IPA and dried with an N2 gun. The samples

were also cleaned using the PlasmaPreen plasma asher at LNL for 30 seconds with Faraday's cage. After that, the samples were dehydrated on a 115°C hotplate for 5 minutes. S1813 positive photoresist was spun on top of the samples using a spinner programmed to 5000 rpm for 63 seconds, followed by a UV exposure for 5.5 seconds. The MJB4 mask aligner at LNL was used for the UV lithography. The photomask that was used contained the semiconductor strip structure needed for the 4P. After exposure, the photoresist was developed by dipping the samples in MF319 developer and stirring for 50 seconds. The samples were thereafter stirred in DIW for 60 seconds. At this point, only photoresist masked from the UV exposure remained, as illustrated in figure 3.1ii. To improve adhesion between the photoresist and the underlying TiO_2 layer, the samples were put on a 120°C hotplate for 10 minutes.

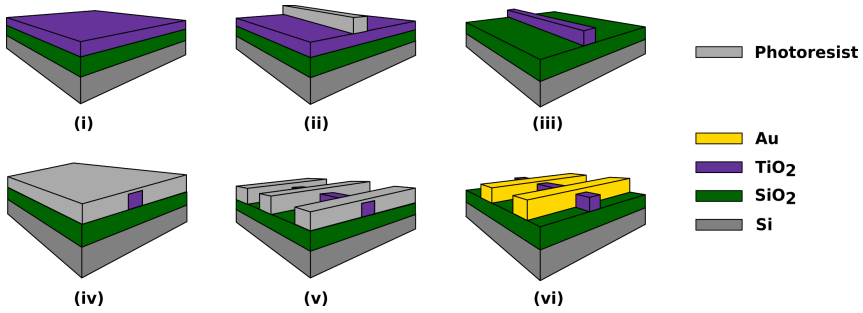

Figure 3.1: Illustration of the sample structures during different stages in the processing. The TiO_2 layer thickness was around 10-20 nm; The dimensions are not to scale.

The samples containing the structured photoresist were dipped into a 1:100 HF solution (48wt% HF:DIW) for 5 minutes to etch the exposed TiO_2. The samples that were subjected to temperatures over 250°C were not etched by the solution. An attempt of etching using hot (90°C) concentrated (98%) sulphuric acid with aluminium oxide as an etching mask was made but without success. The temperature series was thus disregarded for further processing and characterisation. For the remaining samples, an etch rate of approximately 3.8 nm/min was determined by dipping a test sample in the solution in intervals of 1 minute and measuring the thickness using the ellipsometer in between each interval. Using an optical microscope the solution was observed selective to only the TiO_2 layer. The samples were thereafter dried and transferred to a beaker containing remover 1165. The beaker was left on a 90° hotplate, lid on, for 30 minutes to remove the structured resist that was working as an etch mask. Figure 3.1iii illustrates the structure at this point.

The samples were dehydrated on a 110°C hotplate for 5 minutes before a negative photoresist, Ma-N 440, was spun on top. The spinner was programmed to 6000 rpm for 45 seconds. The resist was baked for 3 minutes on a 95°C hotplate followed by a UV exposure for 50 seconds. The mask used in this step contained the structure for the 4P contacts. The photoresist was developed by dipping the samples in MaD 532/s for 105 seconds followed by 60 seconds in DIW. Dissimilar

from the previous positive photoresist used, only the exposed resist in this step remained. Figure 3.1v illustrates the structure at this point.

To remove any resist residues the samples were put in the plasma asher for 30 seconds with Faraday's cage. Using the Temescal E-beam evaporator at LNL, a 5 nm thick titanium followed by a 200 nm gold layer as a top electrode was deposited on top of the sample. The samples were dipped in 70°C acetone for 20 minutes in intervals of 10 minutes to "lift off" the metal layer. The photoresist underneath the Ti-Au layer was dissolved by acetone, detaching the metal layer from the sample. Thus, only in areas without photoresists, does the metal layer remain. To speed up the process, a pipette was used to blow the hot acetone onto the sample after each 10-minute soak. Figure 3.1vi illustrates the structure at this point. The final structure from above, including the probe pads, is also illustrated in figure 3.2. The dashed lines indicate the section illustrated in figure 3.1.

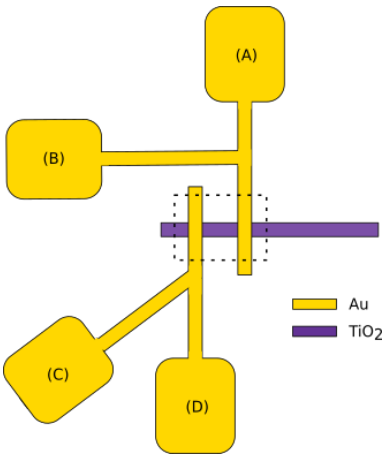

Figure 3.2: The gold structure used for four-probe measurements on the TiO_2 strip

Four-point measurements were carried out using the TS2000-SE semi-auto probe station and the B1500A semiconductor device parameter analyser at EIT. On probe pads A and D, as seen in figure 3.2, a current was sourced and on probe pads B and C the voltage was measured. Using the current sourced and voltage measured the resistance and resistivity were calculated. As shown in the figure, the TiO_2 strip is only connected by two probes, one shared by pad A and B and the other by C and D. The structure is thus not of a four-probe and resistivity could not be calculated correctly. The inner and outer probes are not separated, which is a requirement as discussed in section 2.4.2, and thus the contact resistance could be excluded.

The samples were annealed in the RTP 1200-100 system at LNL for 30 minutes at 300°C. The same four-point measurements prior to the anneal were then carried out.

3.2 Ferroelectric Tunnel Junctions

The heterostructure of the ferroelectric tunnel junctions assembled in this thesis is shown in figure 3.3. TiN and W will be used as bottom and top electrodes, and HZO as the ferroelectric insulator. Since the processing flow contains mostly "bottom-up" techniques, the order of the heterostructure is relevant as the underlying layers will be affected by the ongoing process. This may affect the performance of the FTJ. Therefore, each experiment in this thesis will be conducted twice, once for each order of the heterostructure. The case of TiO_2 as the interfacial layer between the bottom electrode, TiN, and the HZO will be referred to as "bottom TiO_2 and the other case as "top TiO_2", figure 3.3i and 3.3ii respectively. Figure 3.4 illustrates the bottom TiO_2 structure during a few important steps of the process flow.

Using information about the electrical resistivity and GPC of TiO_2 thin films deposited by ALD, acquired from the previous section: "Titanium Dioxide Thin Films", several series of FTJ fabrications were planned. In these series, the TiO_2 deposition conditions were altered. An FTJ without the TiO_2 layer, acting as a reference FTJ, was also made. To investigate the effect of the final oxygen plasma ashing (before electrode sputtering), a sample without said step was made. A reference sample without the ashing step was also made.

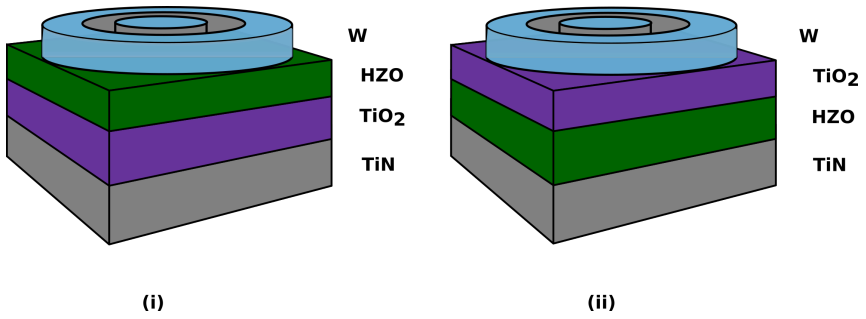

Figure 3.3: The heterostructure of the FTJs constructed in this thesis. The difference between the two images is the placement of the TiO_2 layer. Dimensions are not to scale.

The bottom TiN electrode was formed using the AJA Orion 5 sputterer at LNL. The magnetron was RF powered at 150 W for 10 minutes to form an approximately 10 nm thick layer. Silicon wafers were used as substrate. After this step the wafer was cut into smaller, 1x1 cm, pieces or "dies".

The deposition of HZO was carried out using the Picosun Sunale R-100 ALD tool at LNL. An approximately 4.5 nm thick layer was grown using 45 cycles. The thickness was confirmed using the ellipsometer. The reaction was carried out in 200°C. TEMAZr and TDMAHf were used as the zirconium and hafnium precursor, and water as the oxygen source. The reaction was carried out in 200°C. The deposition was identical for all samples. To induce the orthorhombic phase,

a 50 nm thick layer of W was sputtered on top of the HZO using the AJA Orion 5 sputterer. The magnetron was DC powered with 100 W. The samples were put in the RTP system and annealed at 600°C for 30 seconds. The W layer was, thereafter, wet etched away by dipping the samples in a 60°C 30% H_2O_2 solution for 1 minute. The samples were also dipped in a 60°C 25% NH_4OH solution for 1 minute to etch any W oxides formed.

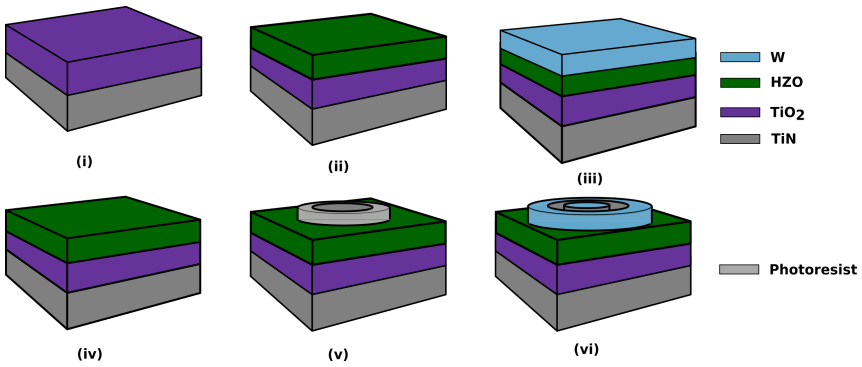

Figure 3.4: Illustration of the FTJ sample structure during different stages in the processing. Important to note is that the TiO_2 is placed beneath the HZO layer, *i.e.* a bottom TiO_2 FTJ.

To form the W top electrode, the samples were dehydrated on a 110°C hotplate for 5 minutes before a layer of MaN 440 resist was spun on top. The spinner was programmed to 6000 rpm for 45 seconds. The resist was thereafter baked for 3 minutes on a 95°C hotplate followed by a UV exposure for 50 seconds using the MJB4 mask aligner. The photoresist was developed by dipping the samples in MaD 532/s for 105 seconds followed by 60 seconds in DIW. To remove any resist residues, the samples were put in the PlasmaPreen asher for 30 seconds with Faraday's cage. Using the sputterer, a 50 nm thick layer of W top electrode was sputtered on top of the samples. The samples were dipped in 70°C acetone for 1 hour in intervals of 30 minutes to lift off the W overlayer. To speed up the lift-off process, a pipette was used to blow hot acetone onto the samples after each 30-minute soak. The top electrode structure is included in figure 3.3. The structure consists of two electrode pad rings.

The formation of "bottom TiO_2"-FTJs started with bottom TiN electrode layer formation followed by TiO_2 deposition, ferroelectric HZO film formation and lastly top W electrode formation. For "top TiO_2"-FTJs the process was identical except for the ALD deposition being placed after HZO formation.

3.2.1 PUND and IV Sweeps

Polarisation measurements, PUND and IV sweeps, were carried out using the TS2000-SE probe state and the B1500A analyser. Firstly, a high voltage of 15 V was applied to the outer pad rings of two FTJs to break the oxides and thus a

short-circuit was made. Either of the two outer pads can now be used to reach down to the bottom electrode (TiN) layer.

Using a script in the B1500A analyser, PUND measurements containing five triangular voltage pulses of 1.5 V and 0.9 ms were applied to one of the outer rings and an inner ring of another FTJ nearby. The PUND scheme is illustrated in figure 4.13viii. Using the B1500A analyser, an IV sweep was carried out to -1.5 and 1.5 V. The TER was calculated from these sweeps. A similar PUND scheme was repeatedly applied 10000 times to the FTJ to allow for wake-up to occur. Identical PUND measurements and IV sweeps were thereafter carried out. From the PUND measurements, the PE curve could be calculated and plotted.

Chapter 4

Results and Analysis

In this chapter, firstly the process series and the results given by the characterisation methods will be presented. Comparisons and trends will also be identified to aid the discussion in the analysis.

4.1 Titanium Dioxide Thin Films

In the first series, the titanium precursor pulse length was increased from 0.2 to 1.1 seconds in steps of 0.3, with 10 seconds of plasma exposure and a reactor temperature of 200°C. In figure 4.1, a boxplot of the GPC for the increasing TDMAT exposure time is shown. The almost equivalent median GPC at 0.8 and 1.1 seconds indicates that surface saturation of the TDMAT molecule has been reached. As mentioned in section 2.3.1, this is a prerequisite for the self-limiting process that allows for thickness control and film uniformity. The dispersion at 1.1 seconds, however, interferes slightly with this hypothesis. Such an increase is not expected but could be due to the characterisation method (ellipsometry) and thus not indicative of a true larger dispersion.

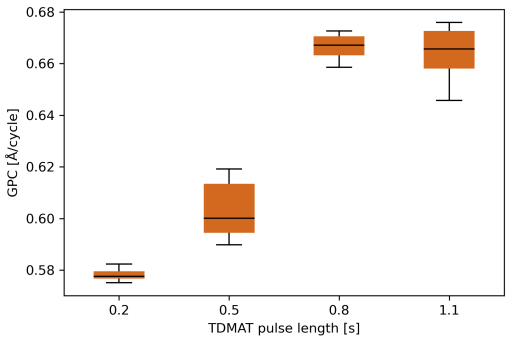

Figure 4.1: Boxplot of the growth per cycle, given in Å/cycle, for the different TDMAT pulse lengths used ALD deposition.

In the second series, the plasma exposure time was increased from 1 to 10 seconds in steps of 3. The TDMAT pulse length was 0.8 seconds and the reactor temperature of 200°C. A boxplot of the GPC for the plasma times is shown in figure 4.2. Saturation could be identified around 7 and 10 seconds given that the GPC does not increase and dispersion decreases. However, the GPC actually decreases which is not expected. The difference in GPC is also small by comparison to shorter plasma times (1 and 4 seconds)

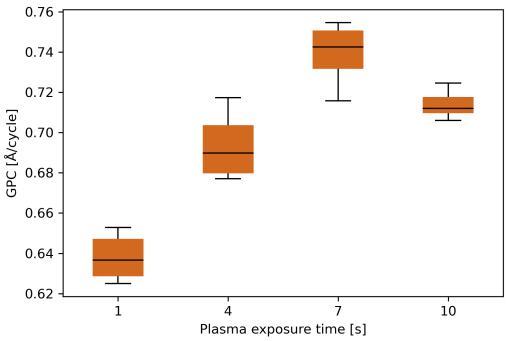

Figure 4.2: Boxplot of the growth per cycle, given in Å/cycle, for the different plasma exposure times used in ALD deposition.

Lastly, in the final series, the temperature was increased from 200 to 300°C in steps of 25°C. The TDMAT pulse length and plasma time were 0.8 and 10 seconds, respectively. The GPC for the temperature series is shown in figure 4.3. In this case, a saturation could be considered at the lower temperatures of 200 to 250°C. At higher temperatures, the GPC increases significantly for which precursor decomposition could be the cause, which is mentioned in section 2.3.1. The film uniformity and phase composition can no longer be controlled.

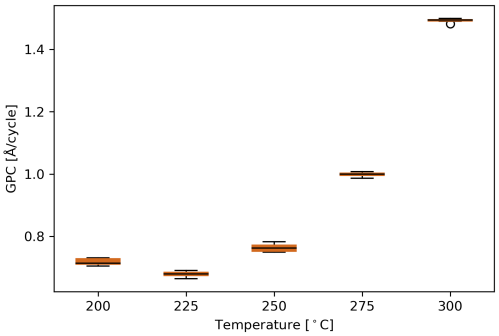

Figure 4.3: Boxplot of the growth per cycle, given in Å/cycle, for the different reactor temperatures used in ALD deposition.

In table 4.1 and 4.2 the resistivity of samples evaluated by the four-probe method, before and after the 300°anneal, are tabulated. The resistivity of most samples can be considered to be on the higher end of the semiconducting regime and bordering pure insulators. A decrease in resistivity is observed due to the high temperature anneal, which is in line with other studies. Annealing increases the grain size resulting in fewer grain boundaries causing scattering [54]. The samples that were deposited with 0.8 and 1.1 seconds of TDMAT pulse lengths post anneal display however a somewhat smaller resistivity of $0.09 M\Omega cm$ and $0.10 M\Omega cm$. The four-probe measurement also revealed that most samples did not exhibit a pure ohmic relation, *i.e.* linear IV curve. As mentioned in the processing details, section 3.1.1, the contact resistances were not able to be excluded in the measurements. This could be the cause of the non-linear dependence. In figure 4.4, examples of both an ohmic and non-ohmic relation from the data are shown. The resistance was calculated from the most linear parts of the graph, indicated by the dashed lines. The preciseness of the measured resistivities is thus questioned. Similar values have, however, been measured in other studies [54].

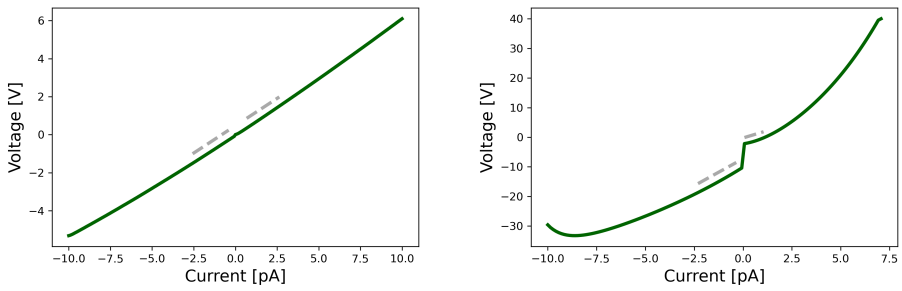

(i) (ii)

Figure 4.4: The sourced current and measured voltage from four-probe measurement of two of the samples; **i** exhibiting an ohmic and **ii** non-ohmic relation. The gray dashed lines indicates the datapoints used to measure the resistance.

As mentioned in section 3.1.1, the samples deposited at temperatures over 250°C were disregarded from further processing and characterisation. The samples were not able to be etched and have thus most likely been crystallised into the anatase phase.

Since the same number of cycles was used for the TiO_2 layer the thickness varied from approximately 11 nm to 30 nm. 11 nm thick TiO_2 layer was grown in the first series with the shortest TDMAT pulse length of 0.2 seconds. The 30 nm thick layer was deposited in the third series with a reactor temperature of 300 °C.

Table 4.1: The calculated resistivity from four-probe measurements of TiO_2 semiconductor strips deposited using ALD with varying plasma exposure times. The resistivity after a 300°C 30 minute anneal is included. The TDMAT pulse length was 0.8 seconds and reactor temperature 200°C.

Plasma exposure time (s)	Resistivity pre-anneal [MΩcm]	Resistivity post-anneal [MΩcm]
1	2.62	3.93
4	6.78	5.94
7	2.55	1.84
10	5.01	1.67

Table 4.2: The calculated resistivity from four-probe measurements of TiO_2 semiconductor strips deposited using ALD with varying TDMAT pulse lengths. The resistivity after a 300°C 30 minute anneal is included. The plasma exposure time was 10 seconds and reactor temperature 200°C.

TDMAT pulse length (s)	Resistivity pre-anneal [MΩcm]	Resistivity post-anneal [MΩcm]
0.2	3.94	1.32
0.5	4.91	0.38
0.8	3.61	0.09
1.1	4.25	0.10

4.2 Ferroelectric Tunnel Junctions

As mentioned in section 3.2, several FTJs of varying ALD deposition conditions were constructed; this is summarised in table 4.3. Two reference samples were also made without the TiO_2 layer, *i.e.* only two metal electrodes and the HZO layer. One of the reference samples was not subjected to the final oxygen plasma ashing step prior to top electrode formation.

Table 4.3: The ALD deposition conditions and approximate thickness of TiO_2 layer used in the FTJs.

Sample index	TDMAT pulse length (s)	Plasma exposure (s)	Thickness (nm)	Other
A1(B/T)	0.2	10	1.5	
A2(B/T)	1.1	1	1.5	
A3(B/T)	1.1	10	1.5	
B1(T)	1.1	10	1.5	300°C anneal post-deposition
B2(T)	1.1	1	1.5	300°C anneal post-deposition
B3(T)	1.1	10	1.5	300°C anneal post-deposition
C1(B/T)	1.1	30	1.5	
C2(B/T)	1.1	60	1.5	
D1(B/T)	1.1	10	4	
D2(B/T)	1.1	10	10	
E1(T)	1.1	30	4	TiO_2 placed only on top
E2(T)	1.1	30	10	TiO_2 placed only on top
E2(T)u	1.1	30	10	Without oxygen plasma ashing; TiO_2 placed only on top

Starting with the reference samples, the PUND response, PE curve, and IV curve are shown in figures 4.5 for both with and without the oxygen plasma ashing step. The coercive field and remnant polarisation for the two samples are tabulated in table 4.4. Such high leakage currents were not expected when compared to studies carried out previously by Athle et al. [55]. In the study, a current density of around 3×10^{-2} A/cm^2 was measured at -1.5 V. In this study, a current density of around 24 A/cm^2 was measured at the same bias instead. Since then the status of the relevant instruments has been investigated and irregular depositions have been observed with the Picosun ALD tool. The deposition conditions of the HZO

layer are thus uncertain not only for the reference samples and indicate that a low-resistive HZO has been made. Probably, conductive paths are formed due to a high defect density.

The general effect of the TiO_2 interlayer can still be identified by comparison of the samples with the reference. Since the HZO of the samples with TiO_2 was not subjected to an oxygen ashing step, the data should be compared to the reference sample without said ashing step, *i.e* sample Ru. Both R and Ru have been subjected to the metal capping and post-metallisation anneal treatment and thus a larger remnant polarisation is expected from the reference sample without the ashing step. Sample R shows, however, a hysteresis curve similar to that of ferroelectrics with adjacent TiO_2. The ferroelectrics of both R and Ru is thus going to be used as a comparison.

The reference sample with the ashing shows a surprisingly and unexpectedly large TER in the IV graphs, figure 4.5iii. Since the structure of the reference sample is MIM, the TER should only be defined by the difference in the screening length of the two metal electrodes. Given that the remnant polarisation is similar to that of the TiO_2 samples, the fraction of the ferroelectric orthorhombic phase could be concluded to be unaffected by the ashing step. The increase in TER could thus be the result of an increased asymmetric charge screening or heightened tunnel barrier possibly caused by a tungsten oxide formed. This has been observed in a study by Bégon-Lours et al. [56].

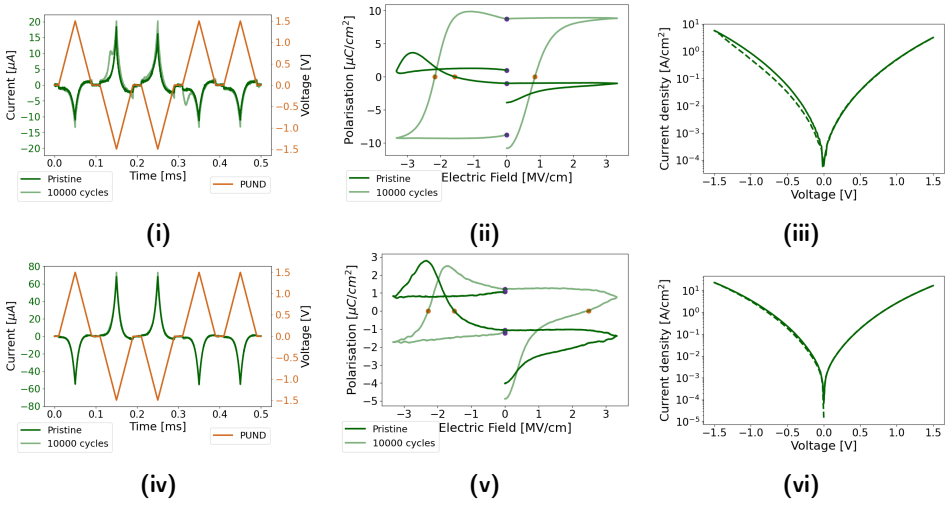

Figure 4.5: The PUND response with calculated PE curve and IV graph for the reference samples with, R **(i)** - **(iii)**, and without, Ru **(iv)** - **(vi)**, the oxygen plasma ashing step. The purple and orange dots in the PE curves display the curves' intersect with $E = 0$ and $P = 0$, and can thus be an indication of the remnant polarisation and coercive field.

In the first series, sample names AX(B/T), three FTJs of varying TDMAT and

Table 4.4: The shifted coercive field (E_{c-} and E_{C+}), remnant polarisation (P_R), and TER for the reference samples after 10000 cycles.

Sample index	$\mathbf{E}_{C-}$ [MV/cm]	$\mathbf{E}_{C+}$ [MV/cm]	$\mathbf{P}_R$ [μC/cm^2]	TER
R	-2.12	0.84	10.13	1.84
Ru	-2.28	2.49	1.22	1.21

plasma pulse lengths were made. Three for each ordering of the structures, AXB or "bottom TiO_2" and AXT or "top TiO_2". The TDMAT and plasma pulse lengths were 0.2 and 10 seconds, 1.1 and 1 seconds, and 1.1 and 10 seconds, corresponding to the extreme values in the previous investigation. The thickness was approximately 1.5 nm. The PUND response, PE curve, and IV curve are shown in figure 4.6 for series AXB and figure 4.7 for series AXT. The coercive field and remnant polarisation are tabulated in table 4.5.

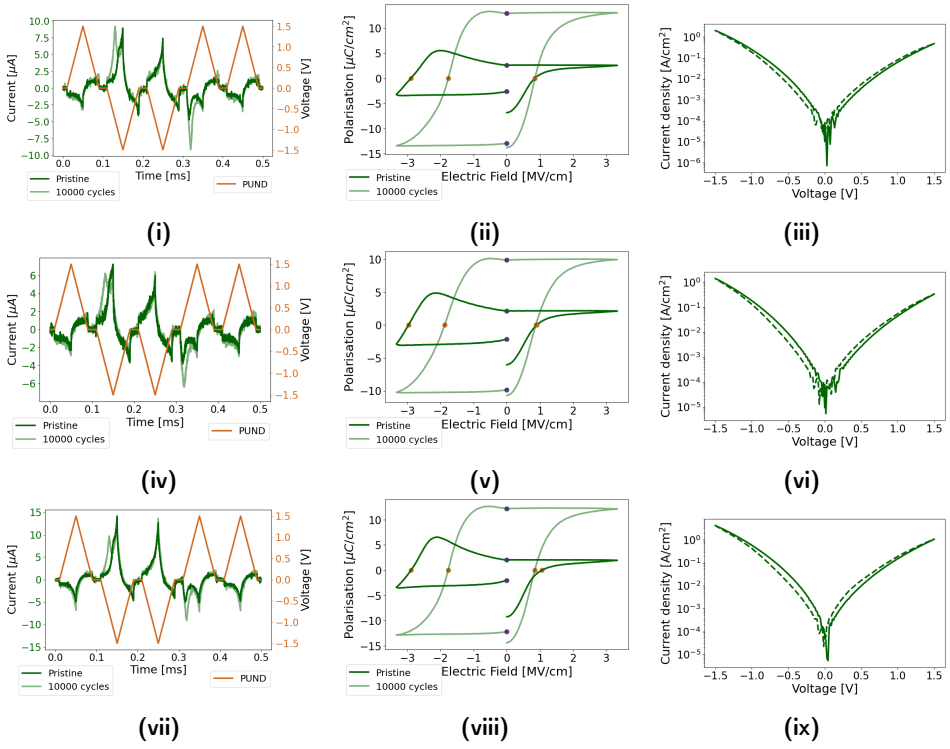

Figure 4.6: The PUND response with calculated PE curve and IV graph for sample A1B **(i)-(iii)**, A2B **(iv)-(vi)**, and A3B **(vii)-(ix)**. The purple and orange dots in the PE curves display the curves' intersect with $E = 0$ and $P = 0$, and can thus be an indication of the remnant polarisation and coercive field.

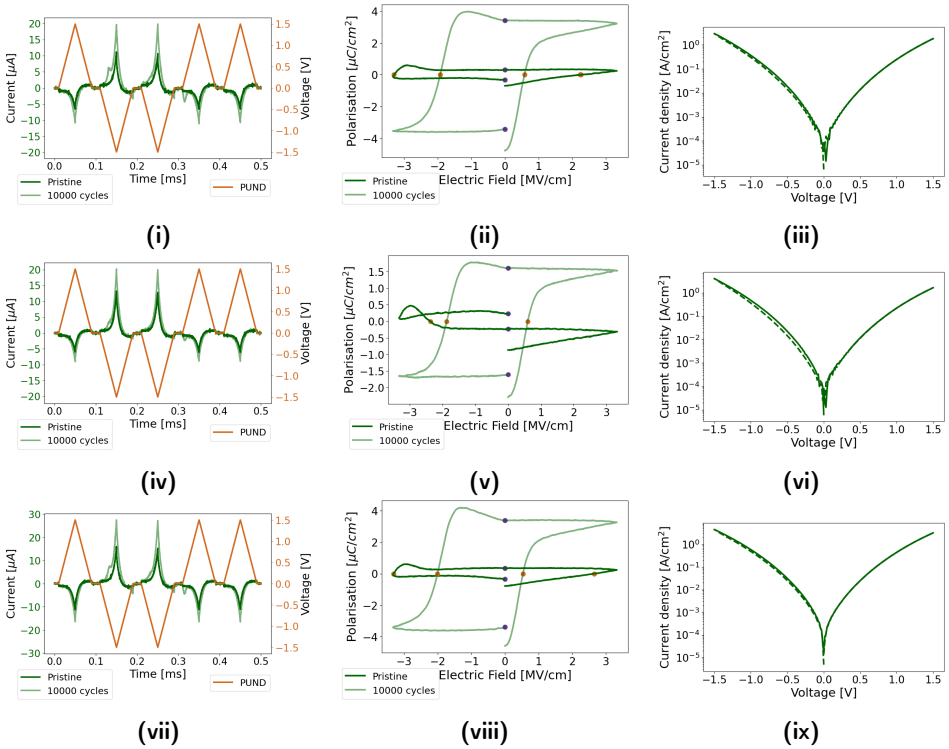

Figure 4.7: The PUND response with calculated PE curve and IV graph for sample A1T **(i)-(iii)**, A2T **(iv)-(vi)**, and A3T **(vii)-(ix)**. The purple and orange dots in the PE curves display the curves' intersect with $E = 0$ and $P = 0$, and can thus be an indication of the remnant polarisation and coercive field.

Table 4.5: The shifted coercive field (E_{c-} and E_{C+}), remnant polarisation (P_R), and TER for sample series AXB and AXT after 10000 cycles.

Sample index	E_{C-} [MV/cm]	E_{C+} [MV/cm]	P_R [μC/cm^2]	TER
A1B	-1.76	0.85	12.88	2.16
A2B	-1.88	0.87	9.85	2.39
A3B	-1.77	0.842	12.18	2.74
A1T	-1.92	0.58	3.42	1.22
A2T	-1.87	0.60	1.61	1.63
A3T	-2.00	0.54	3.37	1.18

In the second series, sample names BXT, identical "top TiO_2"-FTJs to the previous samples were made but a 300°C anneal using the RTP system for 30 minutes after the ALD deposition was included. The PUND response, PE curve, and IV

curve are shown in figure 4.8. The coercive field and remnant polarisation are tabulated in table 4.6. The 300°C anneal can directly be assumed as having little to no effect on the performance of the FTJ since the TER is almost identical. A negligible effect on the ferroelectric properties of the HZO layer is also observed. This is primarily prevalent in the almost identical PE curves.

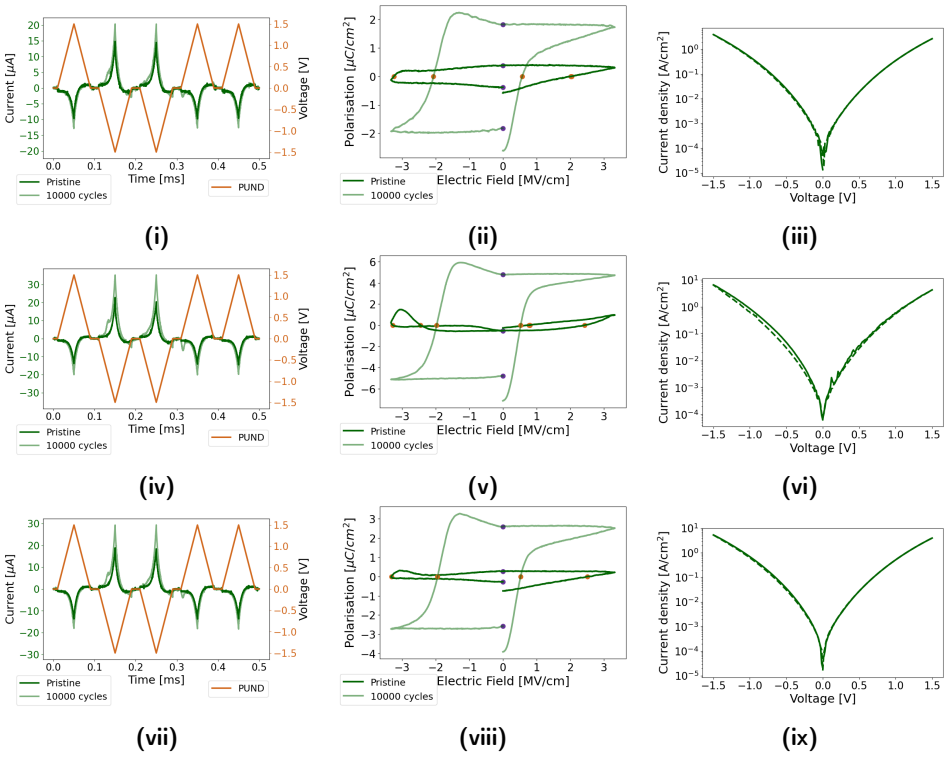

Figure 4.8: The PUND response with calculated PE curve and IV graph for sample B1T **(i)-(iii)**, B2T **(iv)-(vi)**, and B3T **(vii)-(ix)**. The purple and orange dots in the PE curves display the curves' intersect with $E = 0$ and $P = 0$, and can thus be an indication of the remnant polarisation and coercive field.

Table 4.6: The shifted coercive field (E_{c-} and E_{C+}), remnant polarisation (P_R), and TER for sample series BXT after 10000 cycles.

Sample index	$\mathbf{E}_{C-}$ [MV/cm]	$\mathbf{E}_{C+}$ [MV/cm]	$\mathbf{P}_R$ [μC/cm^2]	TER
B1T	-2.06	0.58	1.82	1.10
B2T	-1.97	0.53	4.79	1.68
B3T	-1.94	0.53	2.58	1.09

In the third series, sample names CX(B/T), the plasma pulse length was extended up to 30 and 60 seconds. To stay consistent, the TDMAT pulse length was 1.1 seconds and the thickness was approximately 1.5 nm. Both "bottom TiO_2" and "top TiO_2"-FTJs were constructed. No post-deposition anneal was carried out in this batch. The PUND response, PE curve, and IV curve are shown in figure 4.9 for series CXB and figure 4.10 for series CXT. The coercive field and remnant polarisation are tabulated in table 4.7.

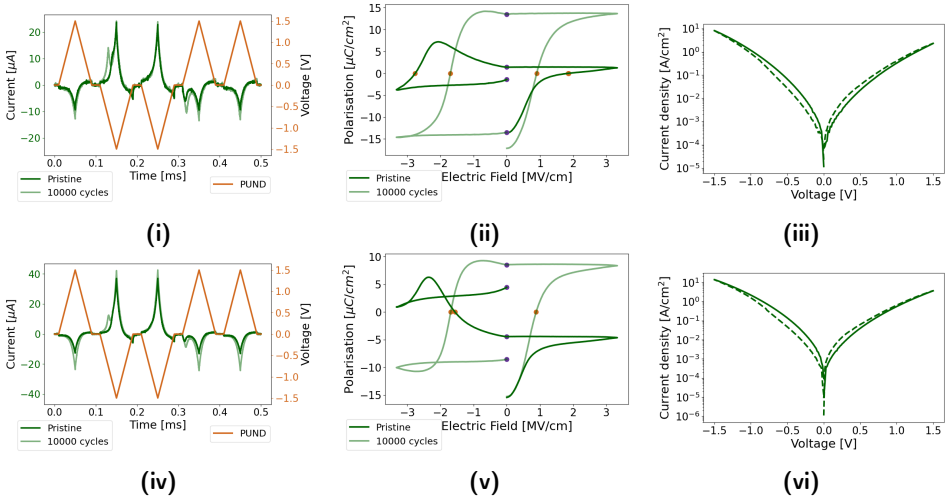

Figure 4.9: The PUND response with calculated PE curve and IV graph for sample C1B **(i)**-**(iii)** and C2B **(iv)**-**(vi)**. The purple and orange dots in the PE curves display the curves' intersect with $E = 0$ and $P = 0$, and can thus be an indication of the remnant polarisation and coercive field.

Table 4.7: The shifted coercive field (E_{c-} and E_{C+}), remnant polarisation (P_R), and TER for sample series CXB and CXT after 10000 cycles.

Sample index	E_{C-} [MV/cm]	E_{C+} [MV/cm]	P_R [μC/cm^2]	TER
C1B	-1.70	0.90	13.52	2.82
C2B	-1.67	0.93	8.65	3.28
C1T	-1.88	0.62	4.12	1.01
C2T	-1.96	0.62	3.46	1.00

So far the data shows that the ferroelectric response is asymmetric as the electric field is swept between the two directions. This is most evident in the shifted PE curves towards negative electric fields. Such a shift is a typical indication of a built-in electric field in the FTJ [57]. To flip the polarisation to one of the directions the applied bias needs to overcome this field. In the other, the fields are added

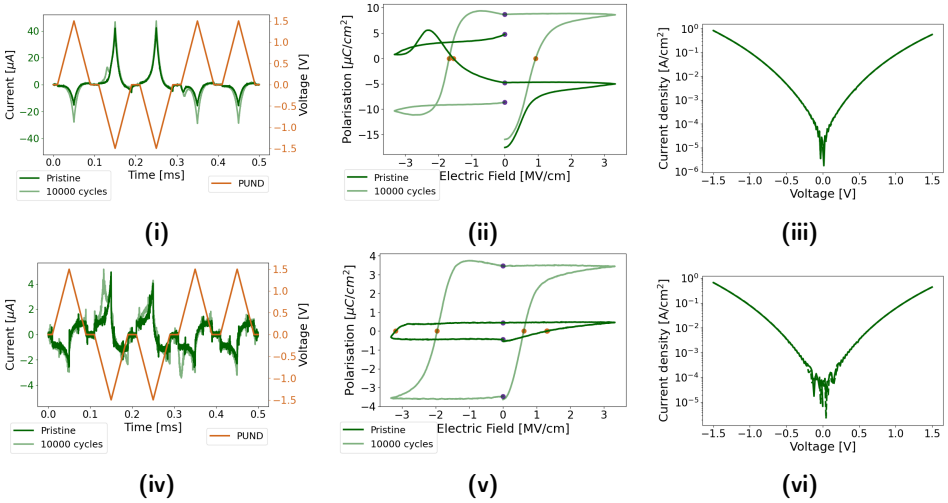

Figure 4.10: The PUND response with calculated PE curve and IV graph for sample C1T **(i)-(iii)** and C2T **(iv)-(vi)**. The purple and orange dots in the PE curves display the curves' intersect with $E = 0$ and $P = 0$, and can thus be an indication of the remnant polarisation and coercive field.

and thus a smaller field is needed to flip.

The built-in field is also observed in the reference samples indicating thus that the faulty deposition is causing the built-in field. Additionally, the charges that would produce the built-in field in FTJ heterostructure could originate from many other different reasons. Firstly, the majority of domains could have been formed in one preferred direction and due to domain pinning the direction remains while switching [58]. The built in field would thus decrease during wake-up. Since the PE curves are plotted after 10000 cycles, this effect should be negligible. Another reason could be piezoelectric effects that occur on the interfaces due to lattice mismatch and broken symmetries [57]. Additionally, there is depletion and accumulation of charge carriers around the junctions and interfaces [59], such as the Schottky junction between HZO and metal electrode, W or TiN. A built-in field could also be produced if the TiO_2 layer is charged. However, all PE curves, either top or bottom TiO_2, are shifted towards negative fields. This implies that for bottom placement, the TiO_2 must be positively charged and negative for top placement. Defects in the crystal lattice, such as oxygen vacancies, could be the reason for the no net charge.

In the fourth series, sample names DX(B/T), the thickness of the TiO_2 layer was increased to approximately 4 and 10 nm. The TDMAT and plasma pulse lengths were 1.1 seconds and 10 seconds. The PUND response, PE curve, and IV curve are shown in figure 4.11 for series DXB and figure 4.12 for DXT. The coercive field and remnant polarisation are tabulated in table 4.8.

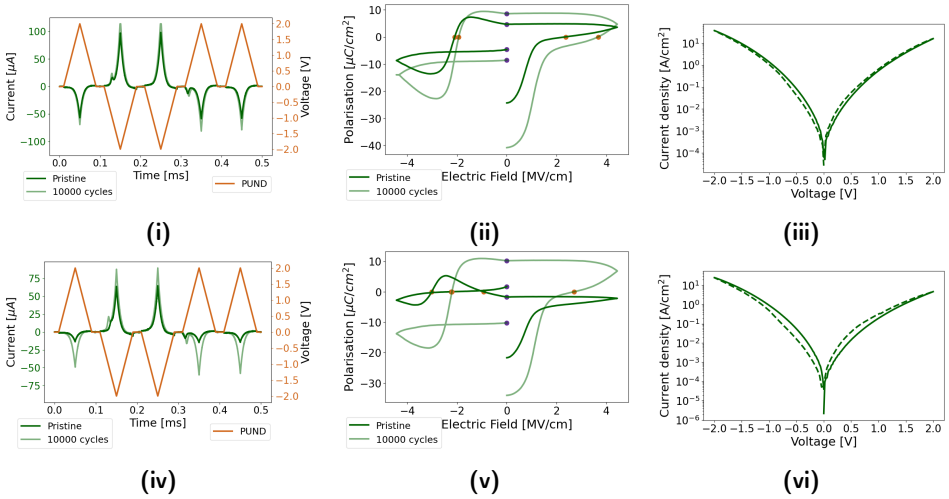

Figure 4.11: The PUND response with calculated PE curve and IV graph for sample D1B **(i)**-**(iii)** and D2B **(iv)**-**(vi)**. The purple and orange dots in the PE curves display the curves' intersect with $E = 0$ and $P = 0$, and can thus be an indication of the remnant polarisation and coercive field.

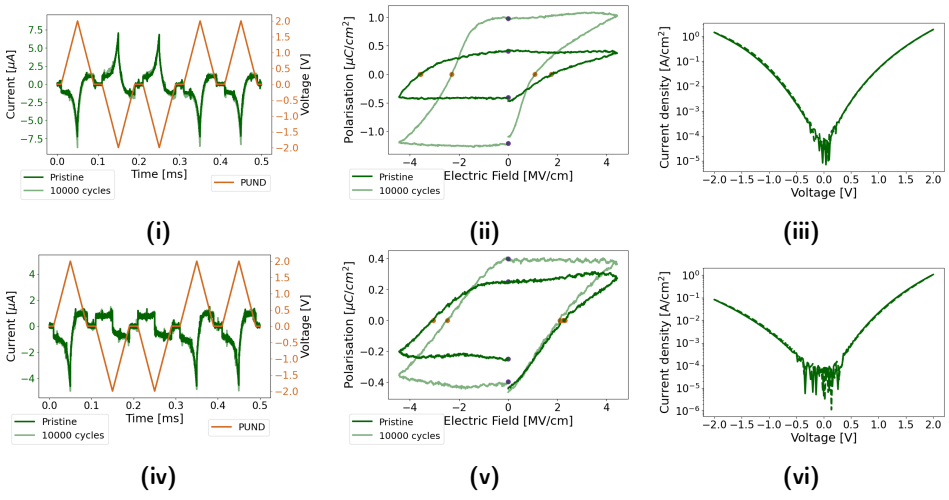

Figure 4.12: The PUND response with calculated PE curve and IV graph for sample D1T **(i)**-**(iii)** and D2T **(iv)**-**(vi)**. The purple and orange dots in the PE curves display the curves' intersect with $E = 0$ and $P = 0$, and can thus be an indication of the remnant polarisation and coercive field.

Table 4.8: The shifted coercive field (E_{c-} and E_{C+}), remnant polarisation (P_R), and TER for sample series DXB and DXT after 10000 cycles.

Sample index	E_{C-} [MV/cm]	E_{C+} [MV/cm]	P_R [μC/cm^2]	TER
D1B	-1.93	3.66	8.55	2.05
D2B	-2.20	2.71	10.21	3.48
D1T	-2.30	1.09	1.21	1.00
D2T	-2.48	2.10	0.40	1.00

In the final series, sample names EXT, the thickness was increased to 4 and 10 nm with a plasma pulse length of 30 seconds. A sample, index E2Tu, was made identical to the 10 nm sample but without the final oxygen plasma ashing step before top electrode formation. The PUND response, PE curve, and IV sweep are shown in figure 4.13. The remnant polarisation and coercive field are tabulated in table 4.9.

Table 4.9: The shifted coercive field (E_{c-} and E_{C+}), remnant polarisation (P_R), and TER for sample series EXT and sample E2Tu after 10000 cycles.

Sample index	E_{C-} [MV/cm]	E_{C+} [MV/cm]	P_R [μC/cm^2]	TER
E1T	-2.11	2.01	0.39	1.00
E2T	-2.45	3.45	0.33	1.00
E2Tu	-3.43	3.42	0.37	1.00

As with the reference samples, the majority of the samples exhibit unexpectedly high leakage currents. As mentioned in section 2.2, the TER is defined as the ratio of the current in two resistive states and is thus promoted by smaller leakage currents. Additionally, a high leakage current is naturally undesired for memory and synaptic device implementation as it elevates power consumption. The leakage currents are summarised in figure 4.14. The current at -1.5 V during the negative IV sweep has been plotted for the different samples corresponding to increasing plasma exposure and TiO_2 thickness. The current here is comprised of both leakage currents and the ferroelectric current response. Only currents after 10 000 cycles are included to ensure that wake-up has happened.

One might be tempted to theorise that the TiO_2 scavenges oxygen from the HZO resulting in conductive paths along the defects, or *trap states*. The steady increase in leakage current with increasing plasma exposure for bottom TiO_2 samples goes, however, against this theory. The extended plasma duration is believed to increase the oxygen concentration at the surface of the film resulting in a *superstoichiometric* TiO_x with x values above 2 [60]. The high content of oxygen in the TiO_2 layer would thus minimise the scavenging of oxygen from HZO.

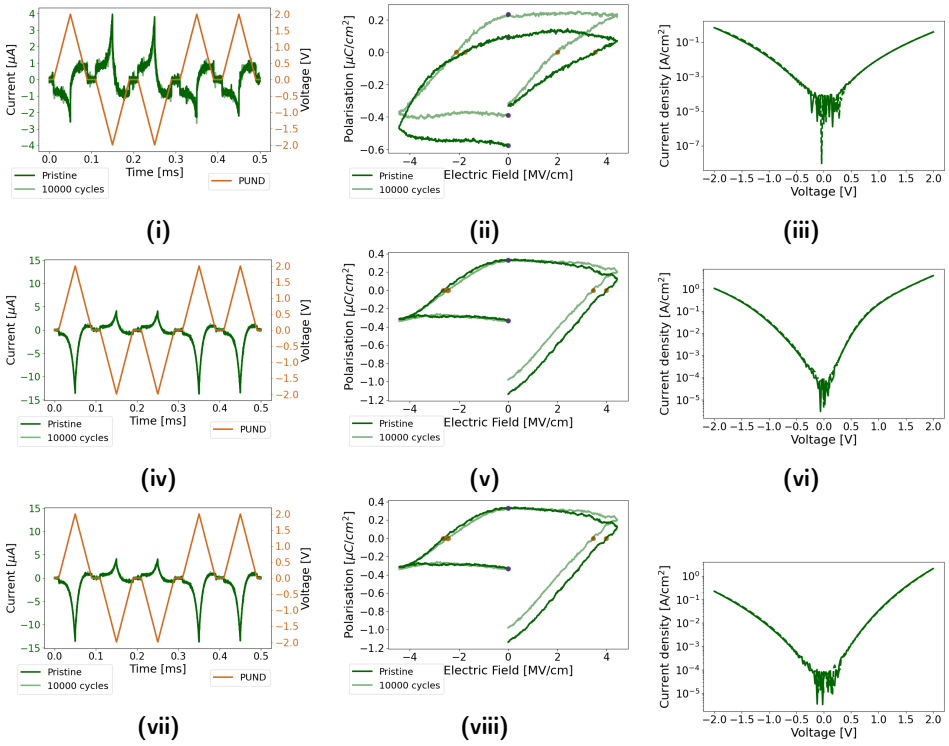

Figure 4.13: The PUND response with calculated PE curve and IV graph for sample E1T **(i)**-**(iii)**, E2T **(iv)**-**(vi)**, and E2Tu **(vii)**-**(ix)**. The purple and orange dots in the PE curves display the curves' intersect with $E = 0$ and $P = 0$, and can thus be an indication of the remnant polarisation and coercive field.

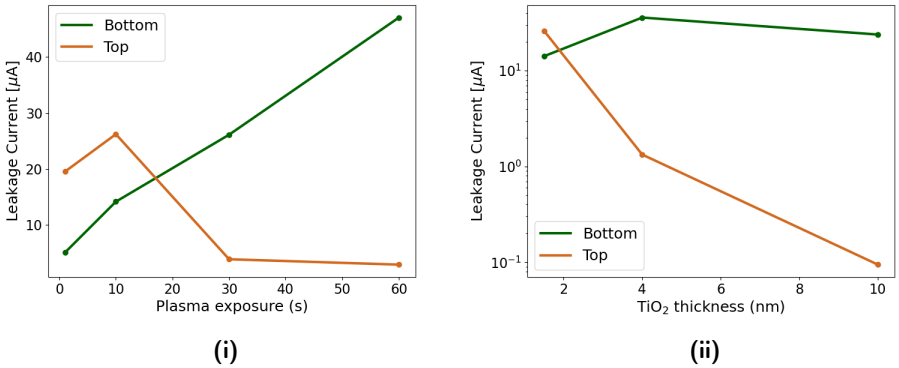

Figure 4.14: The leakage current as function of the **(i)** plasma exposure and **(ii)** TiO_2 thickness. The current was measured during the negative IV sweep at -1.5 V.

The proposing increase in oxygen vacancy defects in the HZO should also affect the properties of the HZO and the performance of the FTJ [61, 62]. As mentioned in section 2.1.7, there is an optimal stoichiometry for the performance. In figure 4.15 the PE hysteresis' dependence on the oxygen plasma is displayed and could be of interest in this theory. For bottom TiO_2 structures, the hysteresis curve barely changes and there is no clear relation between the remnant polarisation and the exposure time. For top TiO_2 structures, similar observations can be made at a higher exposure time. As indicated by the yellow curve, however, the remnant polarisation is considerably smaller for 1 second of plasma exposure time. In a study by Chiappim et al. [60], the superstoichiometric TiOx was identified for a plasma exposure time of 0.25 - 2 seconds. This can thus be an indication that supersaturation is observed for all samples over 1 second of plasma. Thus, the theory of oxygen scavenging from the HZO could be applied to the case of top TiO_2 and 1 second of plasma. The samples of higher plasma (top TiO_2) are already supersaturated with oxygen.

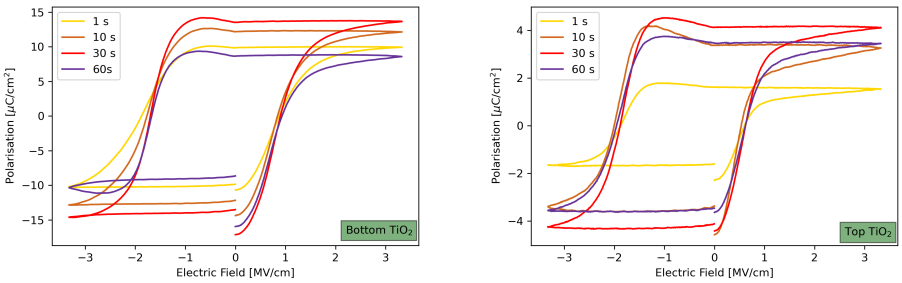

(i) **(ii)**

Figure 4.15: The PE curves from the **(i)** bottom TiO_2 and **(ii)** top TiO_2 samples of varying plasma exposure time in the TiO_2 ALD deposition. The other deposition parameters were identical. The data from samples A2(B/T), A3(B/T), C1(B/T), and C2(B/T) was used.

An opposing theory is mentioned in a study by Martinez et al. [63] and in a study by Brown et al. [64]. For bottom TiO_2 FTJs, the adjacent TiN is theorised to reduce the TiO_2 layer. The TiO_2 is thus deficient in oxygen and the scavenging of oxygen ions from the HZO could be promoted. Examples of reduced states of TiO_x are Ti_2O_3, Ti_3O_5, and TiO. This theory is supported by the 600°anneal that the bottom TiO_2 samples are subjected to. Diffusion is generally expressed with an *Arrhenius equation* and is thus increased exponentially with temperature. An oxygen-deficient TiO_x is also more conductive than the stoichiometric [64] and could thus also partly explain the high leakage currents. This is most prominent for the samples of 10 nm thick TiO_2 from which sourcing such a large current would not be possible if the TiO_2 was a dielectric. The lower resistivity calculated from the four-probe measurements supports this.

The effect of the oxygen concentration in the HZO layer on the ferroelectric prop-

erties is also touched upon by a comparison of the reference samples with and without the final oxygen plasma ashing step. However, the PE curve for the reference sample with the ashing step is similar to that of the samples with TiO_2. The ashing step has thus most likely little to no effect on the oxygen concentration in the HZO. By comparing the ferroelectric properties and FTJ performance of the TiO_2 sample with and without the oxygen ashing step, E2T and E2Tu, the effect of the oxygen concentration in the heterostructure could be further illuminated. The PUND responses and PE curves are almost identical, indicating that the plasma oxygen ashing step has little to no effect. The TiO_2 layer is 10 nm thick and deposited with 30 seconds of oxygen plasma exposure. Little to no effect is thus expected.

As shown in figure 4.14, the leakage currents is drastically decreased with increasing TiO_2 thickness when placed on top but more or less constant when placed on the bottom. This can be explained by the low-resistive HZO layer that is most probably formed due to the faulty deposition. When placed on the bottom, the TiO_2 is subjected to a 600°C anneal resulting in increased grain sizes and lower resistivity. This was observed earlier in section 4.1. In other words, in this case, both the TiO_2 and HZO are low-resistive resulting in the overall high leakage current. For top TiO_2, however, the TiO_2 layer was not subjected to the high temperature anneal and the layer should be semiconducting or even insulating. The resistance through the heterostructure should thus increase noticeably with increasing TiO_2 thickness. As shown in figure 4.14ii this is exactly the case.

The effect of the faulty deposition can also be observed from the PE curves. In figure 4.15 and 4.16, the PE curves are summarised showing the dependence of the curves' appearance on the plasma exposure time and TiO_2 thickness and placement. Assuming the low-resistive (leaking) HZO, most of the applied voltage should fall over the TiO_2 layer placed on top. This is because the TiO_2 layer is more resistive than the leaking HZO. The resulting small voltage drop over the HZO should result in an insufficient electric field for polarisation switching and consequently reduced remnant polarisation. As shown in the figures, this is the case. With increasing TiO_2 thickness a greater part of the voltage falls over the TiO_2 causing even further reduced remnant polarisation. This is observed in specifically figure 4.16ii.

Nonetheless, the PUND responses, PE hysteresis curves, and IV graphs show that the TiO_2 layer, in most cases, improves the performance of the FTJ. The largest TER is found in the IV curve from sample D2B, figure 4.11vi, at approximately 3.5 and from sample C2B, figure 4.9vi at approximately 3.2. The TER of the reference samples is approximately 1.8 and 1.3 with and without the ashing step, respectively. In general, the samples of bottom TiO_2 display superior ferroelectric properties and FTJ performance. Interestingly, the ferroelectric current in the PUND response of samples C1T and C2T, figure 4.10i and 4.10iv, after 10000 cycles are very distinguishable but the TER is close to zero. Once again this is a result of the leaking HZO. The highly conductive paths through defects cause the electron transport to be independent of the barrier shape.

As discussed in section 2.2, the FTJ performance is promoted by using a semi-

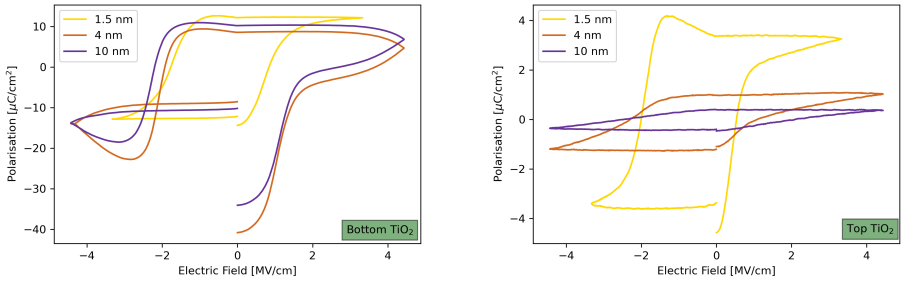

(i) **(ii)**

Figure 4.16: The PE curves from the **(i)** bottom TiO_2 and **(ii)** top TiO_2 samples of varying TiO_2 thickness in the TiO_2 ALD deposition. The other deposition parameters were identical. The data from samples A3(B/T), D1(B/T), and D2(B/T) was used.

conducting electrode due to the barrier modulation resulting in high TER. The top TiO_2 placement should thus be optimal but the performance is limited by the small voltage drop over the HZO caused by the faulty deposition.

Chapter 5

Conclusions

The majority of the results indicate that ferroelectricity has been achieved in the samples and thus TiO_2 is a possible candidate as the semiconductor electrode of ferroelectric tunnel junctions. The TiO_2 layer establishes an asymmetric charge screening between the two polarisation states resulting in a difference in barrier width and thus a resistance contrast. This is most easily concluded from the PUND responses, showing a distinct ferroelectric current peak, and from the PE curves, showing a non-zero remnant polarisation. Irregular deposition of the ferroelectric HZO using the ALD tool was discovered after the thesis work which most likely has affected the result. High leakage currents were observed due to a low-resistive HZO layer and thus limiting the ferroelectric properties. The highest leakage currents were observed for FTJ with a TiO_2 layer placed prior to HZO deposition. By so, the TiO_2 was subjected to a 600°C anneal resulting in lower resistivity. Oxygen scavenging from the TiO_2 by the adjacent TiN electrode could also result in a conductive TiO_2. For TiO_2 placed post HZO deposition, the TiO_2 is assumed still be semiconducting. In this case, however, the FTJ performance was limited due to the low resistive HZO resulting in reduced ferroelectric switching. Greater ferroelectric properties could thus be observed for top TiO_2 samples in future studies when the ALD tool is working correctly.

The highest remnant polarisation displayed in this thesis was 13.52 $\mu C/cm^2$ with an asymmetric coercive field of -1.7 and 0.9 MV/cm. The TiO_2 was deposited under 200°C with 1.1 and 30 seconds of TDMAT pulse length and oxygen plasma exposure time, respectively. The TER of the corresponding FTJ was approximately 2.9.

5.0.1 Outlook

Further analysis of the samples is needed to pinpoint the cause and consequences. A common topic throughout the analysis was the faulty HZO deposition and oxygen vacancies (and other defects), that could result in the high leakages and differences in FTJ performance. Thus, x-ray photoelectric spectroscopy (XPS) would be beneficial in aiding the discussion. In addition, grazing incidence x-ray diffraction (GIXRD) would help determine the crystallographic composition of the HZO layer

and thus the fraction of the ferroelectric phase. Naturally, it would be beneficial to process new samples once the ALD tool is working correctly again.

Other parameters that define the performance of the FTJ, both as a memory element and as an artificial synapse, are also beneficial to investigate. As a memory element, endurance and retention are of prime interest to measure. The switching speed should also be interesting to investigate. As observed in all samples, the leakage current is very high and would thus result in extreme power inefficiency. Solutions, such as modification of the TiO_2 layer's electrical properties, to minimise the leakage current are thus important to discover. Additionally, the FTJs could also be tested as artificial synapses in a simple network. Here it could be beneficial to measure the partial polarisation reversal phenomenon and possibly the ferroelectric domain sizes.

Bibliography

[1] Ferroelectricity in doped hafnium oxide: materials, properties and devices. Woodhead Publishing series in electronic and optical materials. Woodhead Publishing; 2019.

[2] Characterisation of Ferroelectric Bulk Materials and Thin Films. 1st ed. Springer Series in Measurement Science and Technology. Dordrecht: Springer Netherlands: Imprint: Springer; 2014.

[3] Ihlefeld JF. In: Fundamentals of Ferroelectric and Piezoelectric Properties. Elsevier; 2019. p. 1–24. Available from: https://linkinghub.elsevier.com/retrieve/pii/B9780081024300000012.

[4] Mikolajick T, Schroeder U, Slesazeck S. The Past, the Present, and the Future of Ferroelectric Memories. IEEE Transactions on Electron Devices. 2020 Apr;67(4):1434–1443.

[5] Ihlefeld JF. In: Fundamentals of Ferroelectric and Piezoelectric Properties. Elsevier; 2019. p. 1–24. Available from: https://linkinghub.elsevier.com/retrieve/pii/B9780081024300000012.

[6] Fridkin V, Ducharme S. In: Ferroelectricity and Ferroelectric Phase Transition. NanoScience and Technology. Berlin, Heidelberg: Springer Berlin Heidelberg; 2014. p. 1–9. Available from: http://link.springer.com/10.1007/978-3-642-41007-9_1.

[7] Wong CK, Shin FG. A simplified treatment of the Landau theory of phase transitions for thin ferroelectric films. American Journal of Physics. 2008 Jan;76(1):31–38.

[8] Umantsev A. Field Theoretic Method in Phase Transformations. vol. 840 of Lecture Notes in Physics. New York, NY: Springer New York; 2012. Available from: http://link.springer.com/10.1007/978-1-4614-1487-2.

[9] Rabe KM. Physics of ferroelectrics a modern perspective; with 24 tables; 2007. Available from: https://doi.org/10.1007/978-3-540-34591-6.

[10] Chandra P, Littlewood PB. In: A Landau Primer for Ferroelectrics. vol. 105 of Topics in Applied Physics. Berlin, Heidelberg: Springer Berlin Heidelberg; 2007. p. 69–116. Available from: http://link.springer.com/10.1007/978-3-540-34591-6_3.

[11] Tagantsev AK, Cross LE, Fousek J. Domains in ferroic crystals and thin films. New York: Springer; 2010.

[12] Chen A. In: Chen A, Hutchby J, Zhirnov V, Bourianoff G, editors. Electronic Effect Resistive Switching Memories. Chichester, United Kingdom: John Wiley Sons Ltd; 2014. p. 162–180. Available from: https://onlinelibrary.wiley.com/doi/10.1002/9781118958254.ch09.

[13] Fields SS, Smith SW, Ryan PJ, Jaszewski ST, Brummel IA, Salanova A, et al. Phase-Exchange-Driven Wake-Up and Fatigue in Ferroelectric Hafnium Zirconium Oxide Films. ACS Applied Materials Interfaces. 2020 Jun;12(23):26577–26585.

[14] Kim HJ, Park MH, Kim YJ, Lee YH, Moon T, Kim KD, et al. A study on the wake-up effect of ferroelectric Hf 0.5 Zr 0.5 O 2 films by pulse-switching measurement. Nanoscale. 2016;8(3):1383–1389.

[15] Genenko YA, Glaum J, Hoffmann MJ, Albe K. Mechanisms of aging and fatigue in ferroelectrics. Materials Science and Engineering: B. 2015 Feb;192:52–82.

[16] Bégon-Lours L, Halter M, Popoff Y, Offrein BJ. Ferroelectric, Analog Resistive Switching in Back-End-of-Line Compatible TiN/HfZrO 4 /TiO x Junctions. physica status solidi (RRL) – Rapid Research Letters. 2021 May;15(5):2000524.

[17] Böscke TS, Müller J, Bräuhaus D, Schröder U, Böttger U. Ferroelectricity in hafnium oxide thin films. Applied Physics Letters. 2011 Sep;99(10):102903.

[18] Müller J, Böscke TS, Schröder U, Mueller S, Bräuhaus D, Böttger U, et al. Ferroelectricity in Simple Binary ZrO 2 and HfO 2. Nano Letters. 2012 Aug;12(8):4318–4323.

[19] Athle R, Persson AEO, Irish A, Menon H, Timm R, Borg M. Effects of TiN Top Electrode Texturing on Ferroelectricity in Hf 1– x Zr x O 2. ACS Applied Materials Interfaces. 2021 Mar;13(9):11089–11095.

[20] Chen H, Luo H, Yuan X, Zhang D. Realization of excellent ferroelectricity in PDA-derived Hf0.5Zr0.5O2 films through insertion of an ultrathin Ti metal layer. Scripta Materialia. 2022 Aug;217:114758.

[21] Qi Y, Xu X, Krylov I, Eizenberg M. Ferroelectricity of as-deposited HZO fabricated by plasma-enhanced atomic layer deposition at 300 °C by inserting TiO 2 interlayers. Applied Physics Letters. 2021 Jan;118(3):032906.

[22] Park MH, Kim HJ, Do Kim K, Lee YH, Hyun SD, Hwang CS. In: Impact of Zr Content in Atomic Layer Deposited Hf1Zr O2 Thin Films. Elsevier; 2019. p. 75–101. Available from: https://linkinghub.elsevier.com/retrieve/pii/B9780081024300000073.

[23] Park MH, Lee YH, Kim HJ, Schenk T, Lee W, Kim KD, et al. Surface and grain boundary energy as the key enabler of ferroelectricity in nanoscale hafnia-zirconia: a comparison of model and experiment. Nanoscale. 2017;9(28):9973–9986.

[24] Yoong HY, Wu H, Zhao J, Wang H, Guo R, Xiao J, et al. Epitaxial Ferroelectric Hf 0.5 Zr 0.5 O 2 Thin Films and Their Implementations in Memristors for Brain-Inspired Computing. Advanced Functional Materials. 2018 Dec;28(50):1806037.

[25] Wen Z, Li C, Wu D, Li A, Ming N. Ferroelectric-field-effect-enhanced electroresistance in metal/ferroelectric/semiconductor tunnel junctions. Nature Materials. 2013 Jul;12(7):617–621.

[26] Ohlén G. Kvantvärldens fenomen: teori och begrepp. Lund: Studentlitteratur; 2005.

[27] Pantel D, Alexe M. Electroresistance effects in ferroelectric tunnel barriers. Physical Review B. 2010 Oct;82(13):134105.

[28] Velev JP, Burton JD, Zhuravlev MY, Tsymbal EY. Predictive modelling of ferroelectric tunnel junctions. npj Computational Materials. 2016 Nov;2(1):16009.

[29] Gruverman A, Wu D, Lu H, Wang Y, Jang HW, Folkman CM, et al. Tunneling Electroresistance Effect in Ferroelectric Tunnel Junctions at the Nanoscale. Nano Letters. 2009 Oct;9(10):3539–3543.

[30] Sze SM, Lee MK. Semiconductor devices, physics and technology. 3rd ed. Wiley; 2012.

[31] Chua L. Memristor-The missing circuit element. IEEE Transactions on Circuit Theory. 1971;18(5):507–519.

[32] Hasegawa T, Terabe K, Aono M. In: Buschow KHJ, Cahn RW, Flemings MC, Ilschner B, Kramer EJ, Mahajan S, et al., editors. Nanoionics Switching Devices. Oxford: Elsevier; 2011. p. 1–8. Available from: `https://www.sciencedirect.com/science/article/pii/B9780080431529022715`.

[33] Boyn S, Grollier J, Lecerf G, Xu B, Locatelli N, Fusil S, et al. Learning through ferroelectric domain dynamics in solid-state synapses. Nature Communications. 2017 Apr;8(1):14736.

[34] Garcia V, Bibes M. Ferroelectric tunnel junctions for information storage and processing. Nature Communications. 2014 Sep;5(1):4289.

[35] Ma C, Luo Z, Huang W, Zhao L, Chen Q, Lin Y, et al. Sub-nanosecond memristor based on ferroelectric tunnel junction. Nature Communications. 2020 Dec;11(1):1439.

[36] Nature Nanotechnology. 2020 Jul;15(7):507–507.

[37] Boybat I, Le Gallo M, Nandakumar SR, Moraitis T, Parnell T, Tuma T, et al. Neuromorphic computing with multi-memristive synapses. Nature Communications. 2018 Dec;9(1):2514.

[38] Chen L, Wang TY, Dai YW, Cha MY, Zhu H, Sun QQ, et al. Ultra-low power Hf 0.5 Zr 0.5 O 2 based ferroelectric tunnel junction synapses for hardware neural network applications. Nanoscale. 2018;10(33):15826–15833.

[39] Oh S, Hwang H, Yoo IK. Ferroelectric materials for neuromorphic computing. APL Materials. 2019 Sep;7(9):091109.

[40] Mulaosmanovic H, Mikolajick T, Slesazeck S. Accumulative Polarization Reversal in Nanoscale Ferroelectric Transistors. ACS Applied Materials Interfaces. 2018 Jul;10(28):23997–24002.

[41] Martin PM. Handbook of deposition technologies for films and coatings: science, applications and technology. 3rd ed. Elsevier; 2010.

[42] Johnson RW, Hultqvist A, Bent SF. A brief review of atomic layer deposition: from fundamentals to applications. Materials Today. 2014 Jun;17(5):236–246.

[43] Yun J, Park M, Rhee S. Comparison of Tetrakis(dimethylamido)titanium and Tetrakis(diethylamido)titanium as Precursors for Metallorganic Chemical Vapor Deposition of Titanium Nitride. Journal of The Electrochemical Society. 1999 May;146(5):1804–1808.

[44] Lee WJ, Yun EY, Lee HBR, Hong SW, Kwon SH. Dataset for TiN Thin Films Prepared by Plasma-Enhanced Atomic Layer Deposition Using Tetrakis(dimethylamino)titanium (TDMAT) and Titanium Tetrachloride (TiCl4) Precursor. Data in Brief. 2020 Aug;31:105777.

[45] Pakkala A, Putkonen M. In: Atomic Layer Deposition. Elsevier; 2010. p. 364–391. Available from: https://linkinghub.elsevier.com/retrieve/pii/B9780815520313000089.

[46] Martinu L, Zabeida O, Klemberg-Sapieha JE. In: Plasma-Enhanced Chemical Vapor Deposition of Functional Coatings. Elsevier; 2010. p. 392–465. Available from: https://linkinghub.elsevier.com/retrieve/pii/B9780815520313000090.

[47] Madou M, Wang CP. In: Bhushan B, editor. Photolithography. Springer Netherlands; 2016. p. 3157–3166. Available from: https://doi.org/10.1007/978-94-017-9780-1_342.

[48] Ombaba M, Inayat SB, Islam MS. In: Bhushan B, editor. Wet Chemical and Electrochemical Etching Processes. Springer Netherlands; 2016. p. 4373–4380. Available from: https://doi.org/10.1007/978-94-017-9780-1_431.

[49] Shah SI, Jaffari GH, Yassitepe E, Ali B. In: Evaporation. Elsevier; 2010. p. 135–252. Available from: https://linkinghub.elsevier.com/retrieve/pii/B9780815520313000041.

[50] What is RF Sputtering?;. Accessed: 2022-02-28. http://www.semicore.com/news/92-what-is-rf-sputtering#:~:text=RF%20or%20Radio%20Frequency%20Sputtering,the%20plasma%20that%20spews%20droplets.

[51] Ohring M. In: Thin-Film Evaporation Processes. Elsevier; 2002. p. 95–144. Available from: https://linkinghub.elsevier.com/retrieve/pii/B9780125249751500069.

[52] Lindon JC, Tranter GE, Holmes JL. Encyclopedia of spectroscopy and spectrometry. Academic Press; 2000.

[53] Ellipsometry tutorial; 2018. Available from: https://www.jawoollam.com/resources/ellipsometry-tutorial.

[54] Bakri AS, Sahdan MZ, Adriyanto F, Raship NA, Said NDM, Abdullah SA, et al. Effect of annealing temperature of titanium dioxide thin films on structural and electrical properties. Solo, Indonesia; 2017. p. 030030. Available from: http://aip.scitation.org/doi/abs/10.1063/1.4968283.

[55] Athle R, Persson AEO, Troian A, Borg M. Top Electrode Engineering for Freedom in Design and Implementation of Ferroelectric Tunnel Junctions Based on Hf 1– x Zr x O 2. ACS Applied Electronic Materials. 2022 Mar;4(3):1002–1009.

[56] Begon-Lours L, Halter M, Pineda DD, Popoff Y, Bragaglia V, Porta AL, et al. A BEOL Compatible, 2-Terminals, Ferroelectric Analog Non-Volatile Memory. In: 2021 5th IEEE Electron Devices Technology Manufacturing Conference (EDTM). Chengdu, China: IEEE; 2021. p. 1–3. Available from: https://ieeexplore.ieee.org/document/9420886/.

[57] Glinchuk MD, Eliseev EA, Morozovska AN. Influence of Built-In Internal Electric Field on Ferroelectric Film Properties and Phase Diagram. Ferroelectrics. 2007 Aug;354(1):86–98.

[58] Hamouda W, Pancotti A, Lubin C, Tortech L, Richter C, Mikolajick T, et al. Physical chemistry of the TiN/Hf 0.5 Zr 0.5 O 2 interface. Journal of Applied Physics. 2020 Feb;127(6):064105.

[59] Gao P, Nelson CT, Jokisaari JR, Baek SH, Bark CW, Zhang Y, et al. Revealing the role of defects in ferroelectric switching with atomic resolution. Nature Communications. 2011 Sep;2(1):591.

[60] Chiappim W, Fraga MA, Maciel HS, Pessoa RS. An Experimental and Theoretical Study of the Impact of the Precursor Pulse Time on the Growth Per Cycle and Crystallinity Quality of TiO2 Thin Films Grown by ALD and PEALD Technique. Frontiers in Mechanical Engineering. 2020 Oct;6:551085.

[61] Goh Y, Cho SH, Park SHK, Jeon S. Oxygen vacancy control as a strategy to achieve highly reliable hafnia ferroelectrics using oxide electrode. Nanoscale. 2020;12(16):9024–9031.

[62] International Electron Devices Meeting IoE, Engineers E. 2020 IEEE International Electron Devices Meeting (IEDM): 12-18 Dec. 2020.; 2020. Available from: https://ieeexplore.ieee.org/servlet/opac?punumber=9371868.

[63] Martinez J, Sinnott SB, Phillpot SR. Adhesion and diffusion at TiN/TiO2 interfaces: A first principles study. Computational Materials Science. 2017 Apr;130:249–256.

[64] Brown SL, Rossnagel SM, Bruley J, Copel M, Hopstaken MJP, Narayanan V, et al. Oxygen migration in TiO2-based higher-k gate stacks. Journal of Applied Physics. 2010 Mar;107(5):054102.